Journal of CO2 Utilization 70 (2023) 102425

Contents lists available at ScienceDirect

Journal of CO2 Utilization

journal homepage: www.elsevier.com/locate/jcou

Fabrication of highly active and stable Ni/CeO_2-nanorods wash-coated on ceramic NZP structured catalysts for scaled-up CO_2 methanation

Georgios Varvoutis [a,*,1], Athanasios Lampropoulos [a], Paraskevi Oikonomou [b], Constantina-Dia Andreouli [b], Vassilis Stathopoulos [b,c], Maria Lykaki [d], George E. Marnellos [a,e], Michalis Konsolakis [d,*,1]

[a] *Department of Mechanical Engineering, University of Western Macedonia, Kozani, Greece*
[b] *Materials Industrial Research and Technology Center S.A., Chalkida, Greece*
[c] *Laboratory of Chemistry and Materials Technology, Department of Agricultural Development, Agrofood and Management of Natural Resources, National and Kapodistrian University of Athens, Psachna Campus, 34400 Evia, Greece*
[d] *School of Production Engineering and Management, Technical University of Crete, Chania, Greece*
[e] *Chemical Process & Energy Resources Institute, Centre for Research & Technology Hellas, Thessaloniki, Greece*

ARTICLE INFO

Keywords:
CO_2 methanation
Ni/CeO_2
NZP ceramic substrate
Structured catalyst
Scale-up process

ABSTRACT

The production of synthetic natural gas from CO_2 methanation using green H_2 produced via water electrolysis is a promising pathway regarding both the curtailment of excess power by variable renewables and the mitigation of CO_2 emissions. Several catalytic systems have been employed for thermocatalytic CO_2 methanation in lab-scale, with Ni-based catalysts being amongst the most cost-effective and active materials. In this regard, we have recently demonstrated the remarkable low-temperature CO_2 methanation activity of a nickel catalyst supported on ceria nanorods, ascribed to the augmented metal-support synergy. Herein, we report on a scaled-up process of CO_2 methanation, involving; i) fabrication of a highly porous NZP-type ceramic substrate of $Ba_{1+x}Zr_4P_{6-2x}Si_{2x}O_{24}$ in the form of extruded pellets, ii) wash-coating of Ni/CeO_2-nanorods catalyst on NZP pellets, iii) design and testing of scaled-up experiments under a scaling factor of 80:1 and 65:1 in terms of mass and volume of catalysts compared to lab-scale experiments, respectively. The as-synthesized catalyst exhibited remarkable performance under variable reaction conditions and stable behavior after 75 h. Remarkably, the structured catalyst attained a methane formation rate of 277 NL g_{Ni}^{-1} h^{-1}, being higher to numerous values reported in relevant works. Equally importantly, it was disclosed that increased values of space velocity led to high temperature gradient in the catalytic bed, thereby favoring the generation of CO. Intriguingly, the morphological and structural characteristics of the used catalyst remained unaltered even after various on/off reaction cycles and the stability test, which is a promising finding toward scaling-up the process at higher technology readiness levels using real feed streams.

1. Introduction

The scientific community worldwide has been shifting its attention towards effectively mitigating the increasing amount of carbon dioxide that has been accumulated in the atmosphere after decades of intensified anthropogenic activity. Indeed, the elevated levels of atmospheric CO_2 have proven to be detrimental with regards to changes in the climate of the planet, as CO_2 is the dominant gas causing the greenhouse effect. This has been recently highlighted by the detailed report on global climate change by the Intergovernmental Panel on Climate Change (IPCC) [1]. In this regard, aside from the evident benefits of larger penetration of renewable energy sources in the future energy mix, complete decarbonization on a global level is practically infeasible in the medium-to-long term. Thus, it is imperative that the unavoidable CO_2 emissions are valorized in an effective and sustainable manner. Aiming towards this goal, the general scheme of Carbon Capture and Utilization (CCU) is one of the most attractive routes for effectively reducing the carbon footprint of various industrial sectors and eventually producing

---

* Corresponding authors.

E-mail addresses: gvarvoutis@uowm.gr (G. Varvoutis), mkonsolakis@tuc.gr (M. Konsolakis).

[1] The two authors have the same contribution to this study.

https://doi.org/10.1016/j.jcou.2023.102425
Received 12 October 2022; Received in revised form 24 January 2023; Accepted 3 February 2023

value-added chemicals and/or fuels [2,3].

In practice, the hydrogenation of CO_2 is among the most promising CCU routes. From an environmental standpoint, this scheme necessitates that excess renewable energy is transformed into hydrogen via water electrolysis and that the capture of CO_2 from the flue gases of hard-to-abate industries like iron/steel, cement or power plants can be realized in large scales. In this way, a variety of chemicals or fuels can be produced, such as synthetic natural gas (SNG), which is a gas consisting primarily of methane, possessing very similar characteristics (e.g., Wobbe index, heating value) compared to conventional fossil natural gas. Notably, the production of SNG via the so-called CO_2 methanation reaction can effectively stabilize the grid, since SNG can be directly injected in the existing natural gas infrastructure and network [4–6], even with a hydrogen content up to around 10 v/v % [7,8]. This process is commonly referred to as Power-to-Gas and its current status as well as future projects are elaborated elsewhere [9–15]. The reaction of CO_2 methanation is also known as Sabatier reaction and is described by Eq. (1), although the reverse water-gas shift reaction (rWGS, Eq. (2)) may also take place to a certain extent in a H_2/CO_2 feed;.

$$CO_2 + 4H_2 \leftrightarrow CH_4 + 2H_2O,\ \Delta H_{298K} = -\ 164.7\ \text{kJ/mol} \tag{1}$$

$$CO_2 + H_2 \leftrightarrow CO + H_2O,\ \Delta H_{298K} = +\ 41.3\ \text{kJ/mol} \tag{2}$$

It can be seen that the Sabatier reaction is a highly exothermic and mole-reducing chemical reaction, thus it is expected to be thermodynamically favored at low reaction temperature and high reaction pressure, respectively. Nevertheless, in order to overcome both the kinetic barriers, as well as the very high Gibbs energy of the molecule of CO_2 (ca. − 394 kJ/mol) due to the presence of two stable carbon-oxygen double bonds, an appropriate catalyst is a prerequisite for the achievement of high conversion values.

An increased amount of scientific works has been published regarding heterogeneous catalytic systems for the reaction of CO_2 methanation and there are several reviews examining in depth the state-of-the-art systems and their relevant properties and characteristics. In brief, the predominant category of the examined catalysts consists of one or more metallic phases supported on metal oxides [16–21]. However, further elaboration of the optimum catalytic systems is not made herein, as the reader can be referred to the abovementioned reviews. Nonetheless, the role of nickel in CO_2 methanation catalysts simply cannot be overstated, as it is the dominant metal employed as active phase in the relevant literature [22,23]. In this regard, we have recently demonstrated the superiority of Ni compared to other transition metals as well as the key role of metal-support interactions on the intrinsic activity [24,25]. In particular, Ni supported on CeO_2 nanoparticles of rod-like morphology demonstrated an excellent methanation performance (~ 90 % CH_4 yield at 300 °C), being amongst the most active lab-scale, powder catalyst so far reported in the open literature.

Although the examination of a potential catalytic material under controlled lab-scale conditions is of paramount importance in the initial stage of catalyst development, an industrial catalyst needs to be subsequently tested under scaled-up and practical conditions, in order to account for phenomena that are practically negligible in the lab-scale. Most notably, this refers to mass and heat transfer limitations, as well as deactivation effects after several days on stream. In practice, this can only be addressed by the synthesis of the so-called structured catalysts, since the catalyst in the powder form is particularly useful for micro-scale tests to monitor the activity and study the kinetics and mechanism of catalytic reactions in small bed volumes and close to differential conditions. Therefore, there arises the need for the fabrication of structured catalytic composites that need to possess several characteristics prior to their implementation.

Indeed, for rapid and heat-generating reactions, the use of a packed-bed reactor inevitably leads to hot-spots formation and sintering, that are both detrimental for the activity and lifetime of the catalyst. Also, non-uniform flow distribution inside the system results in variable contact times between the active catalyst and the gaseous reactants. In this way and at the regime of low residence time, fixed-bed systems are often associated with a relatively high pressure drop, which is dependent on the particle size, shape and packing of the catalytic material. Although the design of catalysts with smaller particles and thus intrinsically higher activity is favorable from a theoretical viewpoint, this direction is expected to worsen the problems associated with pressure drop, creating several technical difficulties. Thus, macro-structured supporting materials with catalytically active coatings have been gaining attention in chemical engineering as an important part of process intensification, allowing for an efficient mass and heat transfer control, relatively low pressure drop and more degrees of freedom with regards to the final design [26–28]. In essence, the aforementioned structures must possess specific characteristics for their employment as supports in industrial catalysts such as mechanical strength, thermal shock resistance, high heat as well as mass transfer coefficient, high and open porosity, chemical inertness, etc. [27,29,30]. Such features in structured catalysts have been met by ceramic honeycomb monoliths [31,32], foams [33,34], metallic formations, micro-fibrous entrapped catalysts, porous beads, 3D printed and other structures [35–37].

Apart from conventional ceramics (e.g., cordierite, tialite, alumina), materials widely used in structured catalysts at industrial scale, advanced ceramics can provide composition-controlled properties that are suitable for various applications including catalysis. In particular, sodium zirconium phosphates, $NaZr_2P_3O_{12}$, show such interesting properties. This group of materials, widely known as NZPs, was initially studied in the mid-1970s, due to their fast ionic conductivity [38]. Also, due to their ability to accommodate multiple elements in their stable crystal structure, several compounds belonging to the so-called orthophosphate group of $NaZr_2(PO_4)_3$ have emerged as a new class of ceramics [39,40]. NZP materials have a flexible hexagonal crystal structure formed by PO_4 tetrahedra sharing corners along the c-axis with ZrO_6 octahedra. The alkali/alkaline atoms (Na, Ca, Ba, Mg, K, Sr, etc.) are located in the holes between the ZrO_6 octahedra. As a consequence, there is a large number of NZP type compounds containing one to five different cations, capable to tune their properties with composition, such as their thermal expansion and anti-thermal shock properties, their chemical inertness, rendering them as perfect candidates for automobile industry, space or telescope technology [41]. In addition, some NZP members present high mechanical strength, good chemical stability, high melting point, great hardness and radiation resistance [39]. Among the members studied, $Ba_{1+x}Zr_4P_{6-2x}Si_{2x}O_{24}$ has attracted interest as a low thermal expansion ceramic with good mechanical properties at high temperatures, chemical stability and tunable porosity [38]. The above are features required for a material to be employed for the development of a structured catalyst for industrial processes.

Notably, few works examining pilot or semi-pilot experiments of Ni-based structured catalysts for CO_2 methanation exist in the literature. Indicatively, Huynh et al. [31,32], synthesized bimetallic Ni-Fe derived from layered double hydroxides precursors deposited on a cordierite honeycomb substrate and reported a CH_4 yield value of ca. 75 % at 350 °C and at GHSV = 7,760 h^{-1}. Also, Frey et al. [33], reported on enhanced temperature control over aluminum open cell foam catalysts at a bed of 75 cm^3 compared to the powder catalyst, without significant loss in methane production rate. Elsewhere, for tubular Ni-YSZ catalysts synthesized by extrusion molding, enhanced reaction rates were reported, ascribed to a localized hotspot at the inlet due to kinetics/heat generation interplay [34]. Moreover, bench-scale and quasi-adiabatic CO_2 methanation experiments were conducted over a Ni/Gd-CeO_2 catalyst [42]. The active catalytic material was then supported on either a ceramic monolith or an open-cell foam and the crucial role of the support geometry on the temperature profile and on the catalytic activity was revealed. Additionally, the monolith-supported catalyst attained high stability for 50 h during cycles of start-up and shut-down. Lastly, in the work by Ricca et al. [43], the impact of conductive carriers on the temperature profile was highlighted. Specifically, catalysts deposited on either aluminum foam or SiC monoliths were associated with lower temperature gradients compared to the respective powder catalysts, thus maximizing CH_4 yield. Recently, an overview of hydrotalcite-derived catalysts and structured reactors for CO_2 methanation was provided in the review by Huyuh and Yu [44].

In light of the above, in this work a structured catalyst consisting of nickel oxide supported on ceria nanorods as active catalytic material and ceramic NZP as a substrate was developed and assessed catalytically in the scaled-up CO_2 methanation process under variable reaction conditions. The methodology employed herein is summarized in Scheme 1. To the best of the authors' understanding, no such study exists in the relevant literature, which highlights the originality of the present work.

2. Experimental

2.1. Materials synthesis

2.1.1. Synthesis of powder Ni/CeO_2-NR

The powder catalytic material (denoted as Ni/CeO_2-NR) was synthesized via the procedure described in our previous work [25]. In brief, ceria nanoparticles of rod-like morphology (CeO_2-NR) were initially synthesized by the hydrothermal method, followed by Ni incorporation into CeO_2-NR support via the wet impregnation technique, to obtain a Ni/Ce atomic ratio of 0.25, which corresponds to a Ni nominal content of ca. 8.0 wt.%.

2.1.2. Preparation of NZP substrate

The fabrication of the patented ceramic substrate referred to as NZP was carried out in three steps according to our previous publications concerning the preparation of Si-doped barium zirconium phosphate, a typical member of the NZP ceramics group [38,41]. In the first step, the nominal composition of $Ba_{1+x}Zr_4P_{6-2x}Si_{2x}O_{24}$ (with $x = 0.27$) was prepared by reaction sintering of stoichiometric amounts of $BaCO_3$ (Fluka, 98.5 % purity), ZrO_2 (UNITEC), $(NH_4)H_2PO_4$ (Merck, 99 % purity) and SiO_2 (Alfa Aesar). The precursor powders were mixed and calcined at 900 °C. In the second step, the as-prepared NZP precursor was powdered and an extrudable mass was produced with appropriate organic additives and water. The mass was extruded as rods of outside diameter of 3 mm. Pellets were cut in a typical length of 10 mm, dried at 110 °C and in the final step they were fired at 1450 °C in order to obtain the final ceramic substrate used for the deposition of the catalytic wash-coat (Fig. 1a).

2.1.3. Preparation of Ni/CeO_2-NR wash-coats

For the deposition of Ni/CeO_2-NR wash-coats, a stable suspension of the catalytically active material, i.e., Ni/CeO_2-NR, was prepared. Ni/CeO_2-NR powder was ball-milled in the presence of an ammonium polymethacrylate solution (1 wt.%), Darvan C, as the dispersing agent in water. The as-prepared suspension consisting of 10 wt.% in solids was further used for the wash-coat deposition by dipping NZP-type pellets under a vacuum of ca. $1 \cdot 10^{-3}$ Torr. The viscosity of the suspension as well as its stability and re-dispersion properties were controlled accordingly. For the wash-coat deposition, NZP-type pellets air-dried at 110 °C were used. Dipping was repeated until the establishment of the required catalyst loading. The drying step at 110 °C was applied after every dipping. Specifically, six dipping cycles resulted in a Ni/CeO_2-NR loading of ca. 10 wt%, corresponding to an overall nominal Ni loading of ~ 0.8 wt%. Lastly, a final thermal treatment step was carried out at 400 °C for 2 h. The employed composition on a mass basis was equal to 10 % Ni/CeO_2-NR and 90 % NZP substrate and the wash-coated pellet catalyst can be seen in Fig. 1b.

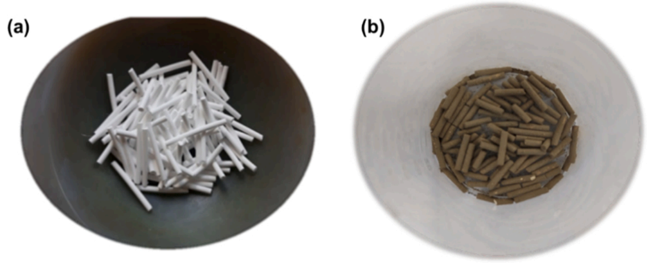

Fig. 1. Extruded NZP-type pellets after annealing (a) and after wash-coating with Ni/CeO_2-NR (b).

2.2. Materials characterization

The actual nickel loading of the non-coated and coated samples was determined by Inductively Coupled Plasma-Atomic Emission Spectroscopy (ICP-AES) in an Agilent 7500 apparatus, after applying microwave digestion with nitric acid. Specific surface area and pore diameter were measured by N_2 physisorption experiments at liquid nitrogen temperature using a Micromeritics Tristar 3000 (Micromeritics, Norcross, GA, USA) using the Brunauer-Emmett-Teller method, after outgassing overnight under vacuum at 250 °C. Morphological and surface analysis was performed by scanning electron microscopy (JEOL JSM-6390LV, JEOL Ltd., Akishima, Tokyo, Japan) operating at 20 keV, equipped with an energy dispersive X-ray spectrometry (EDS) system and transmission electron microscopy (TEM) on a JEM-2100 instrument (JEOL, Tokyo, Japan), equipped with LaB_6 filament operating at 200 kV. The sample was prepared ultrasonically for dispersion and a 400 mesh formvar/carbon copper grid (Agar Scientific, Essex, UK) was dipped into the solution for TEM analysis. The nickel particle size and distribution were determined from TEM images using the ImageJ software. Powder X-ray diffraction analysis was conducted by employing a Rigaku diffractometer (model RINT 2000, Tokyo, Japan). The X-rays were

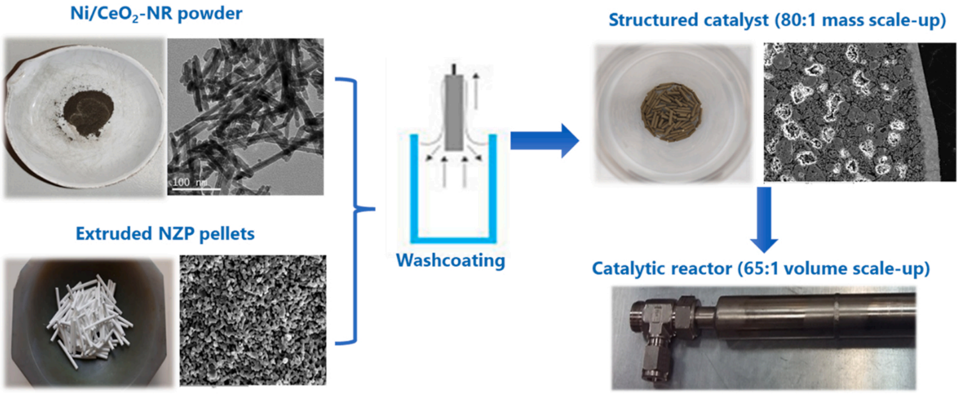

Scheme 1. Structured catalyst development methodology.

produced by a 12-kW rotating anode generator with a Cu anode equipped with a secondary pyrolytic graphite monochromator. A Cu Kα radiation with wavelength $\lambda = 0.154$ nm was used. Measurements were performed with a $\theta/2\theta$ configuration, scanning from 10° to 80° with a step of 0.05°/min. Density measurements were realized via helium pycnometry, whereas the viscosity of the suspension was measured in a Brookfield DVII+Pro apparatus. The initial ball milling for the synthesis of NZP-type powder precursor was evaluated by particle size analysis, carried out in a Laser Diffraction Particle Size Analyzer MASTER Sizer 2000G (Malvern Instruments, United Kingdom) with water as a dispersion medium. After extrusion and firing, the as-formed ceramic pellets were evaluated for their porosity employing the Archimedes method, whereas the sample density was measured via helium pycnometry.

2.3. Catalytic evaluation

2.3.1. Lab-scale experiments

In general, catalytic evaluation experiments of the powder samples were conducted at atmospheric pressure and in the temperature range of 200–500 °C in a quartz fixed-bed U-shaped reactor, placed inside a temperature-controlled furnace. The average bed volume was maintained at ca. 0.30 cm^3 by diluting the catalyst with inert SiO_2 (200 mg each). The reactant gases, consisting of high-purity H_2 and CO_2 (99.999 %) supplied and certified by Air Liquide, were fed at the stoichiometric ratio of H_2:CO_2 = 4 with a flow of 100 mL/min, corresponding to a space velocity of 30 L g^{-1} h^{-1} or ca. 24,400 h^{-1}. The analysis of the gases was performed by a gas chromatograph, while a cold trap submerged in a water bath was connected to the reactor effluent for water condensation.

2.3.2. Scaled-up experiments

The sizing of the stainless-steel catalytic reactor for the scaled-up experiments was based on a mass and volume scaling factor of 80:1 and 65:1, respectively. In this regard, the total mass of the structured composite (i.e., substrate + catalyst) was 15.3 g and the reactor was designed so as to obtain a bed volume of approximately 20 cm^3, corresponding to a bed length of 10 cm. The scaled-up catalytic experiments were conducted in a fully automated flow apparatus comprised of a control and automation system based on a programmable logic controller and a feed system including all the ancillary/auxiliary equipment and periphery instruments (Fig. S1a). The PID of the unit is depicted in Fig. S1b. Gas flow control was realized by mass flow controllers provided by Bronckhorst, whereas temperature control and monitoring was established via numerous thermocouples positioned in various places along the apparatus. Also, condensation of the produced H_2O was achieved in a typical flash condenser via recirculation of cooling water at around 10 °C. At this point, it must be clarified that all tests were performed with the same batch of structured catalyst in the reactor, i.e., without using fresh batches for each set of experiments.

Lastly, thermodynamic equilibrium calculations and validation of experimental results were performed in Aspen Plus software, using the Soave-Redlich-Kwong equation of state for obtaining the thermophysical properties of the associated gas components and by employing an RStoic block accounting for both the Sabatier and the rWGS reactions for the realization of heat and mass balances. The required input (temperature, flows, molar enthalpies) for the feed stream as well as the product yields were exactly the ones from each respective experiment.

2.3.2.1. Effect of inlet temperature and space velocity. Firstly, the catalyst was activated by in-situ reduction with pure H_2 at 400 °C for 1 h and was subsequently cooled naturally in room temperature under inert N_2 flow, following the exact pre-treatment procedure employed in the lab-scale experiments. Then, the effect of inlet temperature (T_{inlet} at the start of catalyst bed, $x = 0$) and gas hourly space velocity (GHSV, in units of h^{-1}) on activity/selectivity performance was explored. In this regard, a certain volumetric flow rate of H_2+CO_2 (between 2.41 and 7.20 NL/min, depending on the experiment) flowed through the preheater and the reactor bed and the oven temperature were set accordingly, in order to reach the desired temperature (i.e., 250, 300, 350 and 400 °C) at the inlet point of the catalytic bed (i.e., at $x = 0$). The same procedure was followed for the three different examined values of GHSV (namely 8,200, 16,500 and 24,400 h^{-1}) by changing the inlet flow rate. Upon reaching and stabilizing at the desired inlet temperature, the system was maintained at each state for approximately 2 h, in order to ensure the establishment of steady-state conditions throughout the bed. At all experiments the ratio H_2:CO_2 was kept constant at the stoichiometric value of 4.

2.3.2.2. Effect of step changes in space velocity. For this experiment, the H_2:CO_2 ratio was equal to 4 and the temperature in the preheater and the oven was kept constant at 300 °C under N_2 flow. Upon stabilization of the system, nitrogen flow was cut off and the reaction mixture at a GHSV of 8,200 h^{-1} was fed into the reactor, while the temperature between the positions $x = -1$ and $x = 10$ cm along the reactor length was continuously monitored at intervals of 1 cm to obtain the full bed temperature profile. After 3 h on stream, the volumetric flow in the reactor (keeping the same H_2:CO_2 feed ratio of 4) was instantly changed to the one corresponding to GHSV = 16,500 h^{-1}, maintained at this condition for another 3 h and the flow was changed one last time to reach a space velocity of GHSV = 24,400 h^{-1}. After the final 3 h on stream, H_2/CO_2 flow was interrupted and the reactor was left to cool naturally until room temperature under N_2 atmosphere.

2.3.2.3. Effect of step changes in the H_2:CO_2 ratio. The effect of reactant ratio was assessed isothermally at 300 °C by gradually varying the H_2:CO_2 ratio from 5 to 3, maintaining a constant gas hourly space velocity of 8,200 h^{-1}. These experimental parameters were chosen in the sense of evaluating the behavior of the catalyst under conditions of either excess or deficit of H_2, since hydrogen provision via RES-powered water electrolysis in a real-scale process is expected to be intermittent, due to variabilities in meteorological conditions affecting solar/wind energy and/or bottlenecks associated with intermediate H_2 storage. As for the selected space velocity, the low value of 8,200 h^{-1} was selected as it was shown herein that is associated with the highest CO_2 conversion value and insignificant temperature gradients in the catalyst bed.

3. Results and discussion

3.1. Materials characterization

3.1.1. Powder catalyst characterization

The powder catalyst was characterized by a variety of methods in our previous work [25], thus herein only a summary of the relevant properties are mentioned (see Table 1). Specifically, ICP-AES analysis demonstrated that the actual nickel content was very close to the nominal value, a finding also corroborated by SEM-EDS analysis. The BET surface area and average pore diameter of the powder catalyst are equal to 72.1 m^2/g and 18.4 nm, respectively. Also, XRD analysis identified the main diffraction peaks of the FCC structure of ceria and cubic nickel. Lastly, TEM analysis clearly evidenced the presence of highly dispersed Ni particles with an average particle size of ca. 10 nm

Table 1
Physicochemical properties of the as-prepared Ni/CeO_2-NR powder.

Ni loading (wt %)		BET area (m^2/g)	Average pore size (nm)	Ni particle size (nm)
7.97[a]	8.06[b]	72.1	18.4	10.4[c]

[a] Measured by ICP-AES.
[b] Calculated by SEM-EDS.
[c] Calculated by TEM.

embedded onto CeO_2 nanoparticles with a distinct rod-like morphology and a length between 50 and 200 nm (Fig. 2).

3.1.2. Structured catalyst characterization

XRD analysis confirmed the formation of a single-phase barium zirconium phosphate silicate crystal structure in the NZP ceramic substrate as well as the crystal phases of NiO and CeO_2 in the catalytic material (Fig. S2). For comparison purposes, a crushed powder sample of the coated NZP ceramic pellets with 10 wt.% Ni/CeO_2-NR catalytic material was also measured by XRD, where the presence of both NZP and CeO_2 phases was confirmed. At the same time, NiO could not be detected due to its low nominal concentration (around 0.8 wt.%), which is below the detection limit. Furthermore, in order to examine the possibility of chemical inertness among the ceramic NZP-type substrate and the catalytic wash-coat, a mixture of NZP and Ni/CeO_2-NR with a 50:50 mass ratio was also prepared. The structural composition of the sample after thermal treatment at 500, 600 and 750 °C for 2 h was detected by XRD analysis. The highest temperature of 750 °C is much higher than the operating temperature of the catalytic bed (see below), albeit sufficient for the investigation of the occurrence of any interaction between the two main phases. Notably, the XRD patterns of the mixture before thermal treatment are similar with those after heating even at 750 °C (Fig. S3**)**. Indeed, the same crystal phases were identified in all three XRD diagrams, i.e., barium zirconium phosphates (NZP) and cerium oxide (CeO_2) with no additional peaks. Again, NiO phase could not be identified due to its low concentration on the investigated samples.

Besides, the acquired values of particle size of the powder NZP-type precursors mixture, d_{50} and d_{90}, were 10 and 20 µm, respectively. Also, the values of the relevant properties of the as-prepared ceramic NZP substrates after annealing can be collectively seen in Table 2. Additionally, the suspension used for the deposition of the catalytic wash-coat was characterized by d_{10}, d_{50} and d_{90} values of 1.23, 2.72 and 6.76 µm, respectively, while its viscosity was measured to be ca. 1.0 cP.

Table 2
Structural properties of the extruded NZP structure after annealing at 1450 °C.

Diameter (mm)	Length (mm)	Porosity (%)	Density (g/cm^3)
1	5–10	51	3.6

Lastly, the morphological characteristics of the ceramic NZP and the wash-coated catalyst were evaluated by SEM analysis (Fig. 3). In all, it is seen that bare NZP is characterized by a homogeneous, sponge-like and highly porous open structure (Fig. 3a), also verified by the cross section image of the pellet (Fig. 3b), showing large and interconnected pore values (Table 2). Also, EDS analysis was conducted in both the outer catalytic layer (Area 1 in Fig. 3b) and the inner ceramic structure (Area 2) and the results are also shown in Fig. 3b. It is evident that the catalytic layer consists of only Ni/CeO_2 at the nominal weight ratio of ca. 8 wt.% Ni, whereas the ceramic substrate consists of Zr, Ba, Si and P, in accordance with the NZP nominal composition. After wash-coat deposition, the formation of a layer of Ni/CeO_2-NR catalytic particles at the outer side of the substrate is evident (Fig. 3c). However, catalytic particles can also be identified in the inner porous structure of the substrate, even at the center of the ceramic pellets. This extent of infiltration can be attributed to the high as well as open porosity (ca. 50 %) with large pores and the sponge-like structure of the ceramic NZP. Such features may facilitate the initial penetration of the finer particles of the wash-coat suspension, even though mass transfer is readily limited by the outer cell formation. In all, these porosity features result in excellent mechanical adhesion of the catalytic nanoparticles over the ceramic substrate.

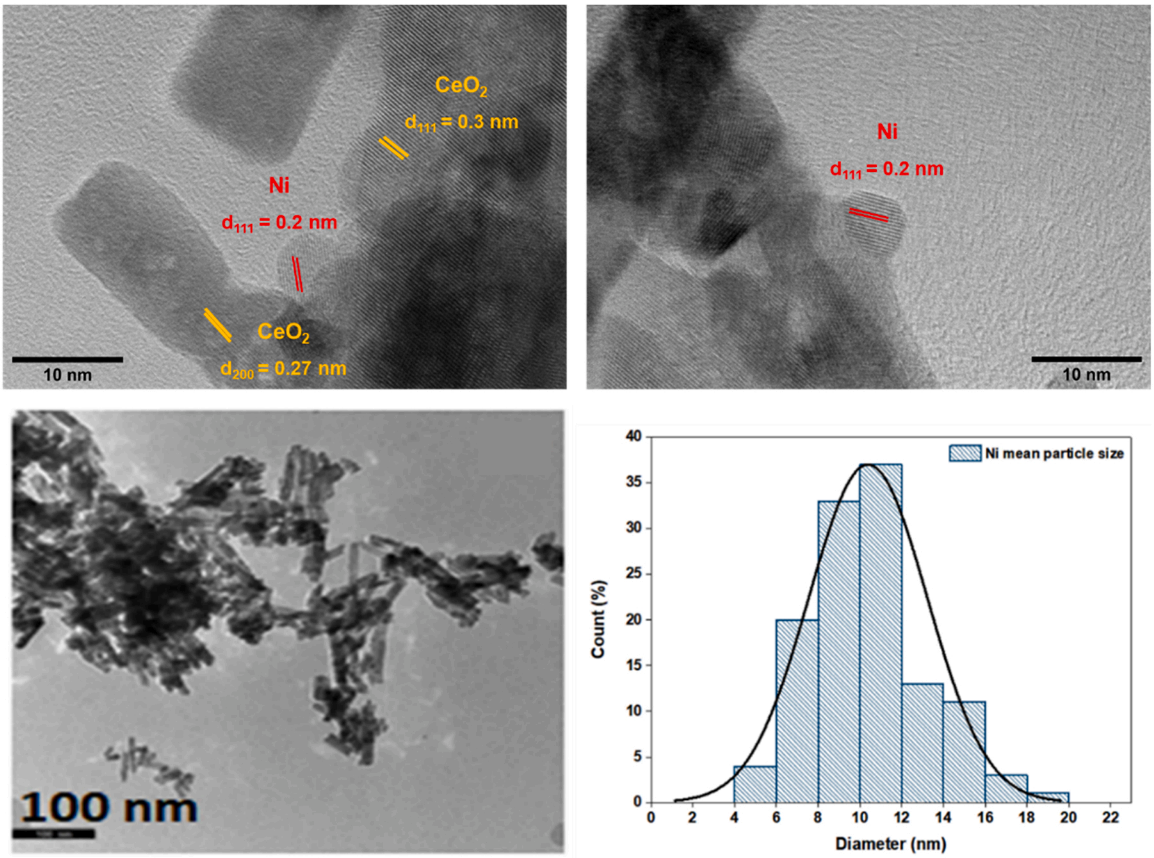

Fig. 2. Indicative TEM images of powder Ni/CeO_2-NR along with Ni particle size distribution. Adapted from Refs. [25,45].

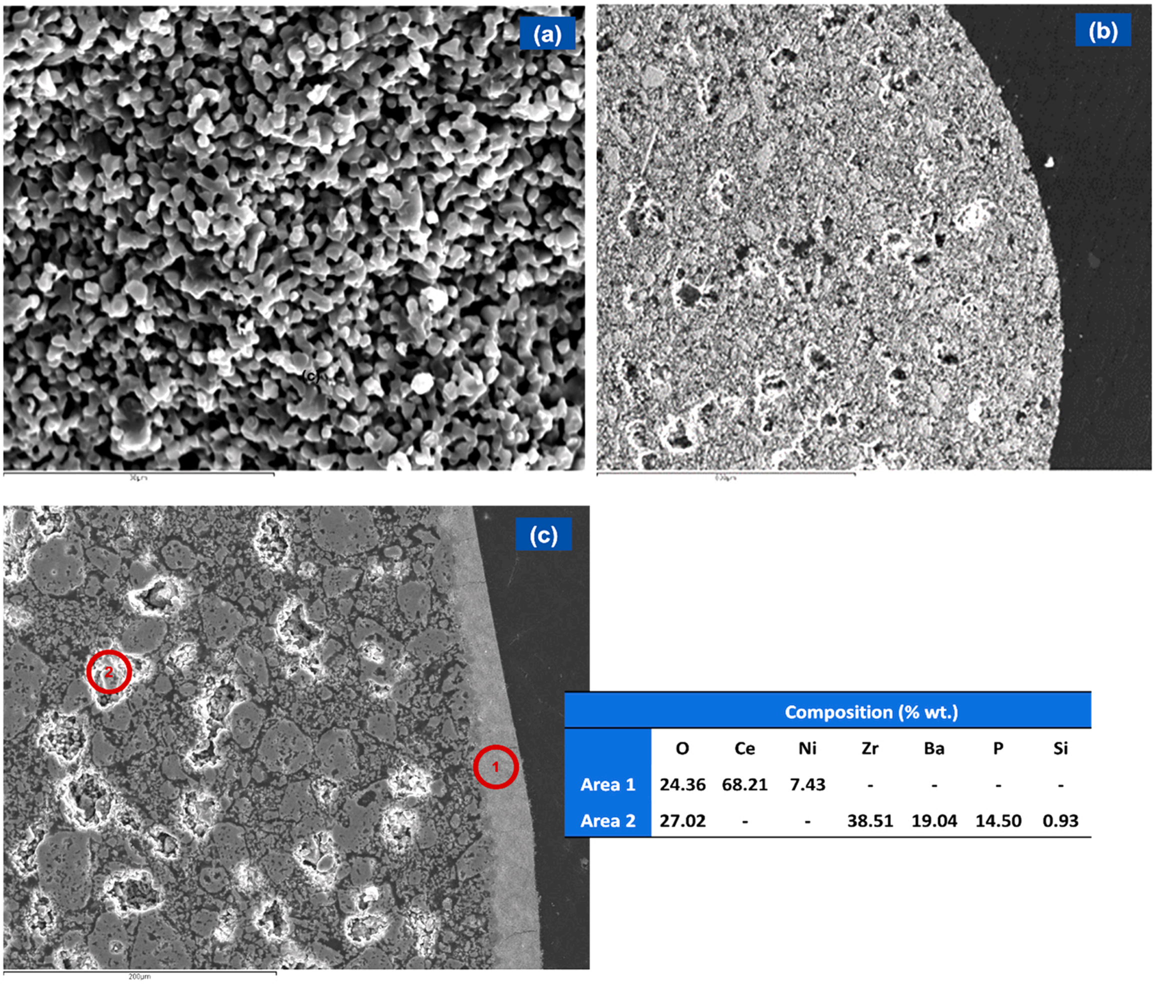

Composition (% wt.)	O	Ce	Ni	Zr	Ba	P	Si
Area 1	24.36	68.21	7.43	-	-	-	-
Area 2	27.02	-	-	38.51	19.04	14.50	0.93

Fig. 3. SEM images of bare NZP pellets (a, b) and after coating with Ni/CeO_2-NR (c). EDS analysis of the inner and outer layer is also shown in (c).

3.2. *Catalytic evaluation*

3.2.1. *Effect of inlet temperature and space velocity*

The results regarding steady-state CO_2 conversion and CO selectivity values (see Section 2.3.2.1) are depicted in Fig. 4. As expected, an increase in the space velocity (or, equivalently, a decrease in the residence time) leads to a decrease in the conversion of CO_2. Also, no significant change was revealed upon increasing the inlet temperature above 300 °C. Notably, a remarkably high CO_2 conversion value of ca. 78 % was attained at 300 °C and a GHSV of 8,200 h^{-1} (Fig. 4a). As far as the product distribution is concerned, at the lowest space velocity of 8,200 h^{-1} methane was practically the only detected product, while the increase in space velocity progressively increased the obtained CO selectivity values, reaching a maximum of ca. 41 % at $T_{inlet} = 400$ °C and at a GHSV of 24,400 h^{-1} (Fig. 4b). The above are also evident when considering the combined effect of both CO_2 conversion and CH_4 selectivity in terms of the CH_4 yield values (Fig. 4c). Clearly, the yield of methane decreases significantly with increasing space velocity, while the effect of the inlet temperature is less prominent.

The latter finding can be explained by accounting for the temperature profiles measured along the catalytic bed, as seen in Fig. 5. The temperature at each point inside the bed was measured by positioning a thermocouple accordingly and waiting until a stable indication was established. Evidently, regardless of the employed space velocity and inlet temperature, a temperature gradient was reported in all experiments, with the highest value reported in the middle of the catalytic bed ($x = 5$ cm). Even more importantly, significantly higher bed temperature values were recorded upon increasing the space velocity, most probably a direct result of the higher volumetric gas flow in the reactor, which transfers more heat lengthwise in the bed. Thus, the higher temperatures measured at a GHSV of 16,500 h^{-1} and especially at 24,400 h^{-1} may be considered as mostly responsible for the increase in CO selectivity, since the rWGS reaction is mildly endothermic and thermodynamically favored at higher temperatures. Indeed, at 24,400 h^{-1}, bed temperatures were as high as 550–600 °C, a range in which the formation of CH_4 is expected to be supressed in favor of increased CO generation, as seen by the corresponding equilibrium lines for each reaction in Fig. 4a. Similar results regarding temperature gradients in the catalytic bed for scaled-up CO_2 methanation have been reported elsewhere [42,43,46,47].

Moreover, to gain insight into the origin of the high catalytic activity of the as-prepared structured composite, the catalytic performance of Ni/CeO_2-NR powder was compared under the same H_2:CO_2 feed ratio and space velocity with that of binary powder catalyst (Ni/NZP) and individual constituent materials (i.e., Ni, CeO_2 and NZP) as well as with a physical mixture of equal amounts of Ni/CeO_2-NR and NZP (denoted as NiCe+NZP) and a powder of the wash-coated pellet (denoted as NiCe/NZP) in lab-scale experiments, as shown in Fig. 6a. It is evident that Ni/CeO_2-NR attains the highest values for CO_2 conversion compared to both the binary Ni/NZP and individual constituents as well as to the physical mixture and the wash-coated powder, indicating the synergistic effect between the nickel phase and the ceria nanorod support, albeit with no obvious interactions between the Ni/CeO_2 catalyst and the NZP substrate. Also, significant differences exist with regards to the product

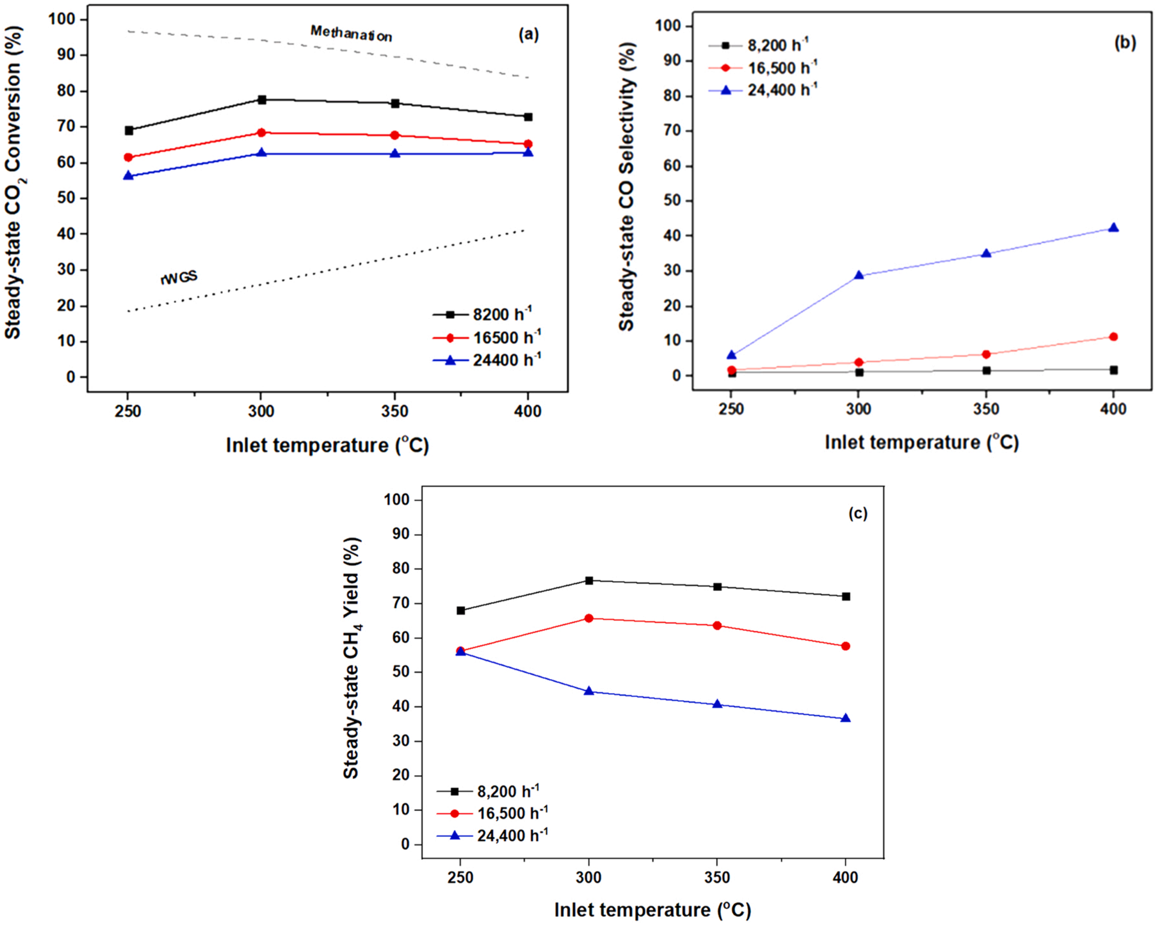

Fig. 4. Effect of the inlet temperature and space velocity in (a) CO_2 conversion, (b) CO selectivity and (c) CH_4 yield values.

distribution, evidenced by the CO selectivity values in Fig. 6b. Obviously, bare ceria nanorods and bare NZP are significantly more selective towards CO compared to the nickel-containing samples, showcasing the synergistic interaction of the nickel active phase and ceria nanorods carrier towards high methane production, as discussed extensively in our relevant works [25,48].

Moreover, for comparison purposes, the results of the pellet catalyst at the same reaction conditions are collectively presented in Fig. 6c, where two different axes for the inlet and maximum bed temperatures are shown, in order to visualize the differences between the set temperature in the inlet and the maximum recorded value in the bed. Besides, although the temperature profile was not monitored in the lab-scale experiments (which were characterized by a typically small bed volume between 0.25 and 0.30 cm^3, thus establishment of isothermal conditions along the bed is assumed), the demonstrated differences in conversion/selectivity between the powder samples and the pellet catalyst can nonetheless be ascribed to the high temperature gradient attained in the case of the structured catalyst (vide infra). Ergo, it is evident that the high temperature gradient in the catalyst bed observed in the scaled-up experiments shifted the actual thermodynamic limitations of the reaction in terms of both CO_2 conversion and product distribution compared to the quasi-isothermal experiments for powder samples. In this regard, the equilibrium conversion lines in the case of powder and structured catalysts are practically different and not directly comparable. Therefore, the selected temperature value for the calculation of the actual equilibrium CO_2 conversion is the steady bed temperature for the former and the maximum bed temperature for the latter. In any case, the respective equilibrium plots for CO_2 methanation and rWGS reactions are also depicted in Fig. 6a and c, respectively.

In light of the above and in order to more meaningfully compare the catalytic performance of Ni/CeO_2-NR (i.e., the optimum powder catalyst) and the pellet sample, the approach to equilibrium metric was next calculated, firstly introduced in our previous work [49] and defined therein as the ratio of the experimental to the thermodynamic CO_2 conversion. Notably, the normalized CO_2 conversion values for both samples are very similar (Fig. 7), indicating that the high activity of the powder catalyst is largely maintained in the structured formulation and under the employed scaled-up conditions away from differential operation. In other words, both the powder as well as the pellet catalyst attain a similarly high catalytic activity in terms of CO_2 conversion upon the initiation of the reaction at the same inlet temperature values, irrespective of the large temperature increase in the case of the pellet catalyst. At the same time, the activated CO_2 in the case of the structured catalyst is partially converted to CO and not exclusively to CH_4, which is a direct result of the development of higher temperature gradients in the bed, an inevitably disfavoring condition for the progression of the exothermic CO_2 methanation reaction, as discussed next.

Indeed, this is better evidenced in Fig. 6d, where the equilibrium CO selectivity values for the inlet and maximum bed temperatures are shown. It is evident that the thermodynamic tendency of the system towards the suppression of CH_4 production at the expense of CO is greater at the temperature regime of the maximum recorded bed temperature in the scaled-up experiments. Thus, it can be reasoned that the pellet catalyst is associated with an inherently high (and similar to the one for the powder catalyst) CO_2-to-CH_4 activity, with the only limitation in elevated methane yield values practically being the temperature increase in the bed under high space velocity, which leads to operation under a CO-favoring temperature range.

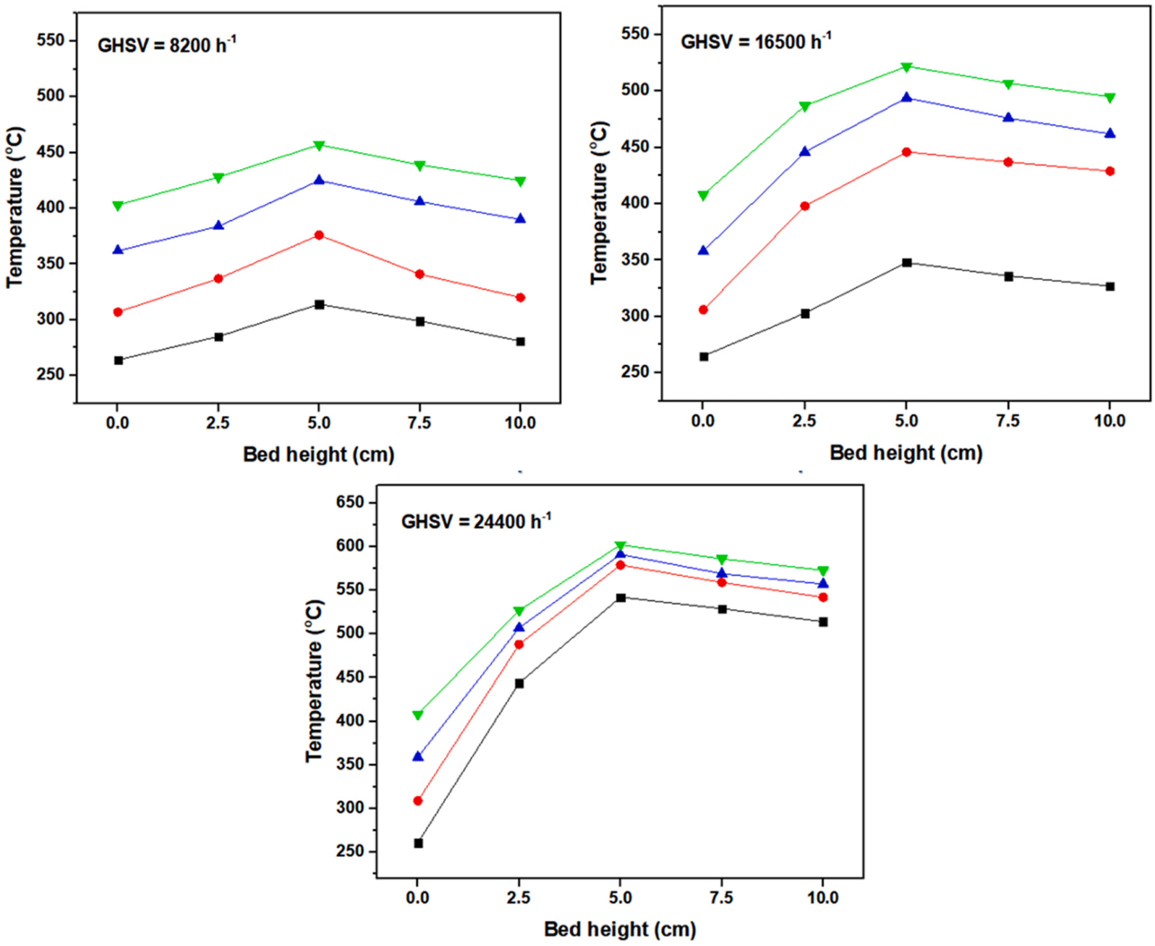

Fig. 5. Temperature profiles along the catalyst bed for various inlet temperature and space velocity values.

Lastly, the powder and pellet catalyst can be further compared by means of the CH_4 productivity normalized per gram of nickel (or similarly per gram of Ni/CeO_2). Indeed, by calculating the respective values at the point of maximum CO_2 conversion for both samples, the pellet catalyst attains a significantly higher rate of ca. 277 NL g_{Ni}^{-1} h^{-1}, as opposed to the value of 53 NL g_{Ni}^{-1} h^{-1} for the powder sample. The performance of the pellet catalyst is higher compared to numerous values reported in relevant works, as summarized in [33] and also in [42,50]. This finding demonstrates that the selection of the wash-coating percentage of 10 wt% was sufficient for the synthesis of an active catalyst structure. Also and with the scope of a further scale-up of the process, this indicates the effective catalytic utilization of nickel in the case of the structured catalyst.

3.2.2. *Effect of step changes in space velocity*

Following the temperature screening in the preliminary experiments, the effect of step changes in space velocity at the temperature for maximum CO_2 conversion was next explored (see Section 2.3.2.2). The corresponding results are depicted in Fig. 8, from which it can be seen that the gradual increase in the space velocity slightly decreased the conversion of CO_2 and at the same time substantially increased the selectivity towards CO (Fig. 8a), essentially attaining the same results at the respective conditions in the previous experiments (Fig. 6a), which is also revealed in terms of methane yield and productivity (Fig. 8b). Not unsurprisingly, the lowest methane productivity was attained in the operation under the lowest space velocity of 8,200 h^{-1}, owing to the low reactant flow into the reactor. However, the significant increase in CH_4 productivity at higher space velocities is indicative of the ability of the system to maintain its high CO_2-to-CH_4 activity under decreased residence time values. Besides, a slight decrease was subsequently observed at the highest space velocity of 24,400 h^{-1}, due to the higher CO selectivity. The latter is in accordance with the first set of experiments and can be directly ascribed to the instant temperature increase along the catalytic bed, as clearly depicted in Fig. 8c and as will be further discussed below.

Moreover, to gain insight into the effect of the temperature gradient along the bed length under different flow rates, the amount of the produced reaction heat was normalized by the difference between the highest recorded temperature in the bed and the one at the exit of the bed (that is, at x = 10 cm), both at steady-state conditions. In this way, a semi-quantitative evaluation of heat evacuation (in units of W/K) from the catalytic bed can be made, as defined in Ref. [33] and denoted herein as H_{ev} (Eq. (3));

$$H_{ev} = \frac{|Q_{rxn}|}{T_{max} - T_{10cm}} \tag{3}$$

The reaction heat, Q_{rxn}, can be calculated by the following expression (Eq. (4));

$$Q_{rxn} = N_{CO_{2,in}} \cdot (\Delta H_{Sabatier} \cdot Y_{CH_4} + \Delta H_{rWGS} \cdot Y_{CO}) \tag{4}$$

where; $N_{CO2,in}$ (in mol/s) is the molar inlet flow of CO_2, ΔH_i (in J/mol) is the enthalpy of the Sabatier and rWGS reactions calculated for the value of the bed inlet temperature and Y_i (%) is the yield of CH_4 and CO. The calculations were validated by a separate simulation in Aspen Plus software. The calculated values of H_{ev} for each space velocity are depicted in Fig. 9. Intriguingly, similar values were calculated for 8,200 and 16,500 h^{-1}, while a significantly higher value was calculated at the

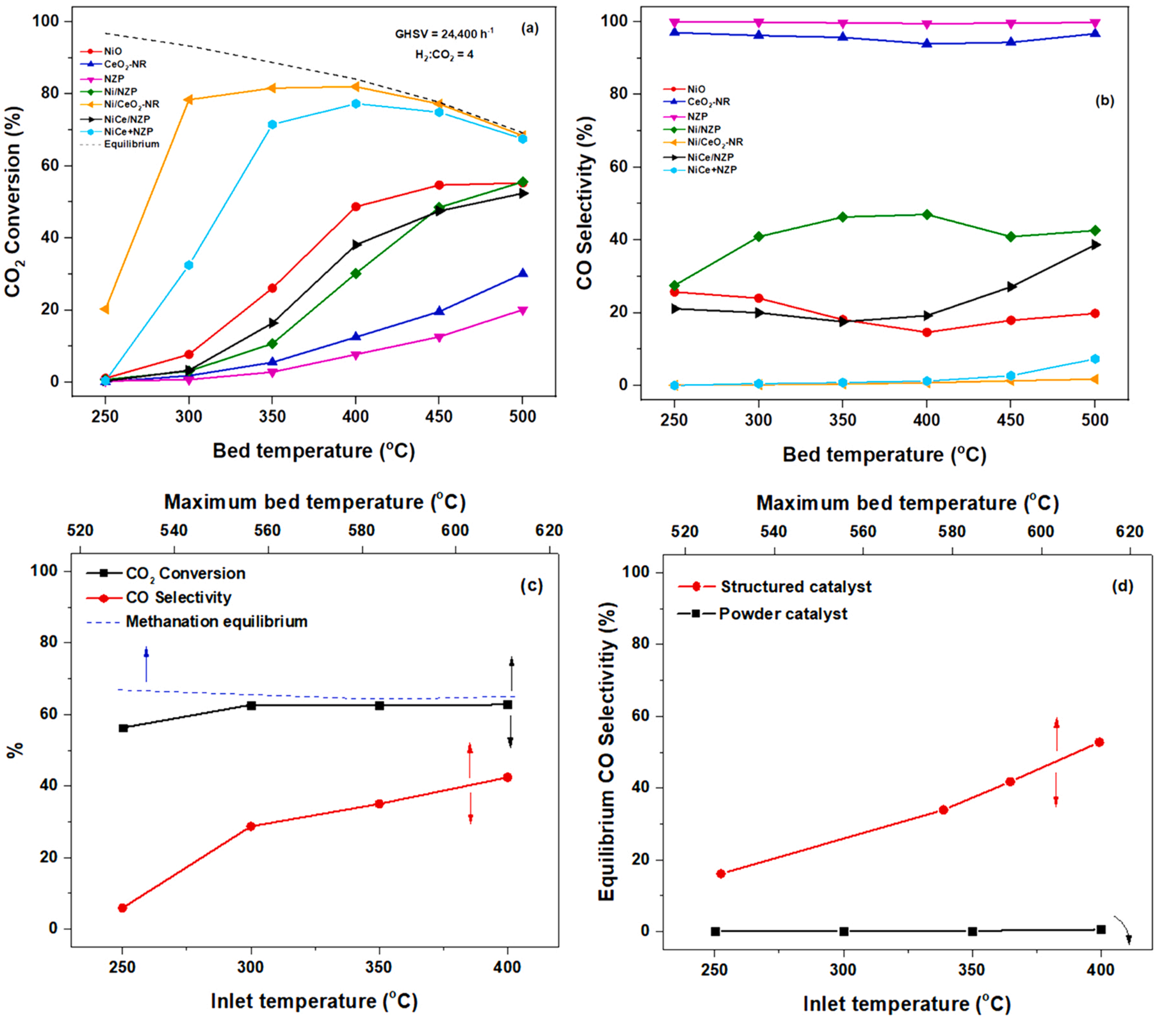

Fig. 6. Comparison of the catalytic performance of powder reference samples (a,b) and pellet structured catalyst (c) and equilibrium CO selectivity for H_2:CO_2 = 4 as a function of the inlet and maximum bed temperatures recorded at 24,400 h^{-1} (d). The bottom and top x-axis in (c) and (d) correspond to the inlet and maximum bed temperature, respectively.

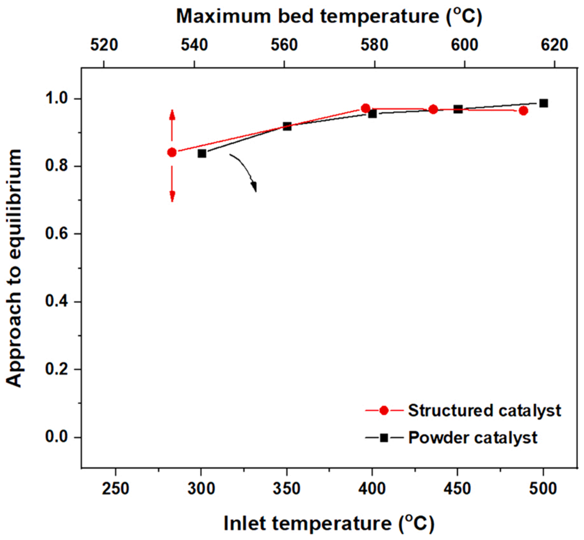

Fig. 7. Approach to equilibrium for the powder Ni/CeO_2-NR and structured catalyst. Reaction conditions; GHSV = 24,400 h^{-1}, H_2:CO_2 = 4.

highest GHSV value of 24,400 h^{-1}, indicating the decreased efficiency of the system in removing the generated heat in the absence of external reactor cooling and under high-GHSV conditions. Even more importantly, the trend following H_{ev} values directly correlates with the observed CO selectivity in Fig. 8b. This showcases that a higher gas flow in the reactor leads to a decreased heat transfer in the axial direction of the bed which in turn is largely detrimental for heat removal capacity. This might be a direct result of the fact that since no external cooling source is provided in the reactor, the system is not able to thermally handle by itself the generated reaction heat via its transfer towards the flowing gases at GHSV = 24,400 h^{-1}. In other words, it could be reasoned that the system operates above the critical gas flow (or equivalently below the critical residence time) that is required in order to effectively absorb and transfer a large part of the produced heat outside the reactor unit at a rate higher than its generation. Therefore, outwards heat dissipation is limited and the catalytic bed sustains higher temperatures that inevitably hinder the production of methane via the exothermic Sabatier reaction and simultaneously increase the yield of CO via the endothermic rWGS reaction.

3.2.3. Effect of step changes in the H_2:CO_2 ratio

The obtained results from the experiment under variable H_2:CO_2 ratios (see Section 2.3.2.3) are depicted in Fig. 10, along with the respective equilibrium values. As expected thermodynamically, an

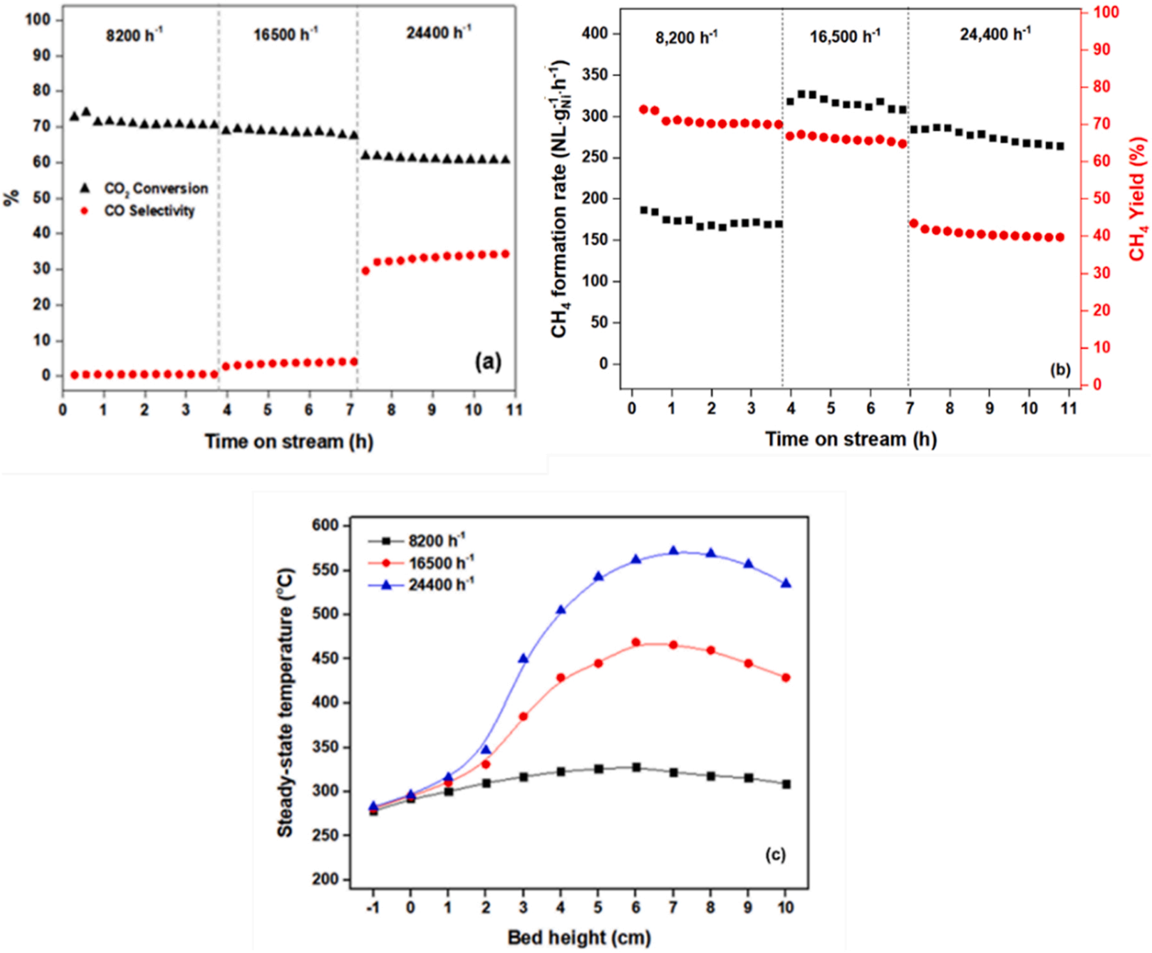

Fig. 8. Effect of step changes in the GHSV on (a) CO_2 conversion/CO selectivity, (b) CH_4 production and (c) bed temperature profile.

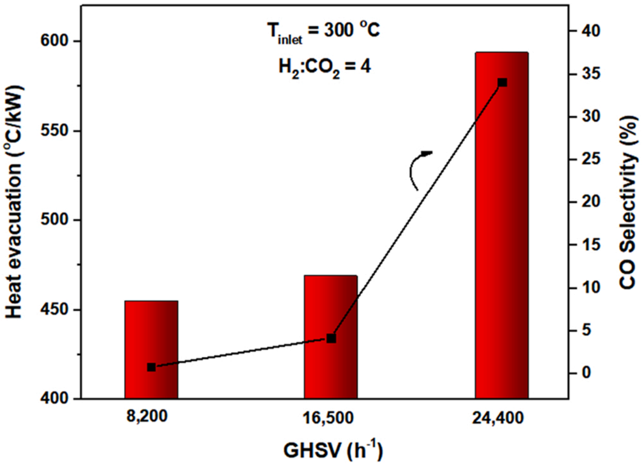

Fig. 9. Heat evacuation values and CO selectivity as a function of space velocity.

increase in the H_2 concentration in the feed favors the conversion of CO_2. More specifically, the highest CO_2 conversion (~ 83 %) was attained at the over-stoichiometric H_2:CO_2 ratio of 5, followed by the one for a ratio of 4 (~ 67 %) and the lowest value of ~ 53 % was reported under sub-stoichiometric conditions, i.e., H_2:CO_2 = 3 (Fig. 10a). In any case, however, the steady-state CO_2 conversion values amounted to ca. 70–80 % of the thermodynamically predicted values, showcasing the high one-pass catalytic activity of the investigated structured sample. Moreover, the selectivity towards CO was negligible and reached its highest value of 3 % under the lowest H_2 inlet concentration. As for the reported temperature gradients in the catalytic bed, it was established in the aforementioned tests that the manifestation of higher temperature gradients (and in turn increased CO generation by the thermodynamically suppressed CO_2 methanation) was a direct result of increased gaseous flow in the reactor, in other words it essentially occurred only under operation at high space velocities. Intriguingly, since the GHSV value employed in this experiment was low, no significant temperature gradients could be monitored along the bed, irrespective of the reactant feed ratio, with the highest temperature measured around the middle of the bed (Fig. 10b). Moreover, considering that higher CO_2 conversion values were attained at the condition of H_2:CO_2 = 5, it is in turn expected that even more heat will be produced owing to the exothermicity of the reaction. So, the establishment of quasi-isothermal conditions in the bed (given that a maximum value of ΔT = 40 °C was measured) is a promising finding in terms of avoiding the generation of hot-spots in the catalytic bed that would likely lead to rapid deactivation, even under increased heat flux from the system outwards.

Moreover, in an analogous analysis for heat evacuation as the one followed in the previous section, the corresponding calculated values are shown in Fig. 11. It is obvious that although different CO_2 conversion values were attained at different feed ratios leading to higher heat generation, the efficiency of heat removal from the bed assessed via the normalized H_{ev} values remains practically constant, irrespective of the employed H_2:CO_2 ratio. Ergo and in conjunction with the results from Fig. 9, it can be reasoned that the reactant ratio exerts practically no

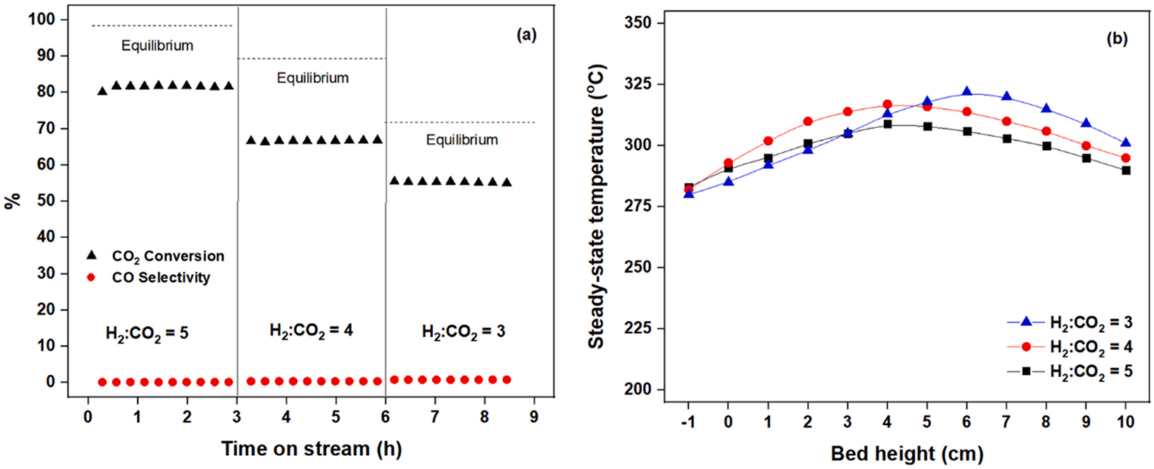

Fig. 10. Effect of step changes in the H_2:CO_2 ratio on CO_2 conversion/CO selectivity (a) and bed temperature profile (b).

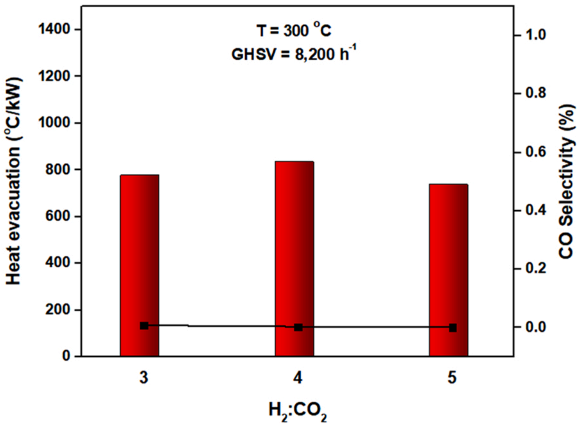

Fig. 11. Heat evacuation values and CO selectivity as a function of the H_2:CO_2 ratio.

difference in the bed temperature profile, as long as the system operates under a low space velocity. In other words, under low gaseous flow, relatively mild temperature gradients are developed in the catalytic bed which are a result of the high efficiency of the system in removing the generated heat outwards from the catalytic bed via its dissipation to the passing gases. Thus, the endothermic rWGS reaction is largely suppressed and low CO selectivity values are observed.

3.2.4. Stability test

As a final means of assessment of the applicability of the as-synthesized structured catalyst, a long-term stability test was conducted. The catalyst sample that was used was the same as in all the previous experiments, i.e., the sample had already been tested for around 55 h in several on/off reaction cycles under variable conditions. Considering the results of the aforementioned reaction condition screening, the experiment was conducted with a stoichiometric H_2:CO_2 ratio equal to 4, a space velocity value of GHSV = 8,200 h^{-1} and at a temperature equal to $T_{preheater} = T_{oven} = 300\ ^\circ C$. The results from the stability test are collectively depicted in Fig. 12. Remarkably, a very stable performance in terms of both CO_2 conversion and CO selectivity were obtained after 75 h on stream, equal to ca. 71 % and 0.5 %, respectively (Fig. 12a). In order to better assess the stability performance of the catalyst, the deactivation rate can be estimated by the following expression (Eq. (5)), assuming first-order kinetics [36,37];

$$k_d = \frac{1}{t}\left[\ln\left(\frac{1-X_t}{X_t}\right) - \ln\left(\frac{1-X_0}{X_0}\right)\right] \tag{5}$$

where; k_d (h^{-1}) is the deactivation rate, t (h) is the duration of the experiment, X_t is the final CO_2 conversion and X_0 is the initial CO_2 conversion, specifically the value obtained after the initial stabilization of the system.

The calculated value of the deactivation rate was $3.30{\bullet}10^{-3}\ h^{-1}$. Whereas there are no reported k_d values for scaled-up CO_2 methanation experiments in the literature, the calculated value herein is almost an order of magnitude lower compared to somewhat indicative lab-scale studies, demonstrating the adequate stability behavior of the as-synthesized pellet catalyst, even upon comparison with results under more ideal, lab-scale conditions [51,52]. Nonetheless, the deactivation rate in this work is no more than an estimation and the actual value should be calculated by long-term stability tests.

Additionally, as seen in Fig. 12b, the critical temperatures in the bed inlet/outlet, as well as the maximum bed temperature remained practically constant throughout the experiment, further showcasing the stable performance of the catalyst and revealing the establishment of thermal steady-state conditions. Also, by averaging the measurements made over the entire 75-h period at intervals of 1 cm in the bed axial direction, the temperature bed profile is depicted in Fig. 12c. Again, the maximum temperature was recorded near the middle of the bed (at x = 6 cm), while a maximum temperature difference of ca. 92 °C was recorded. Moreover, for a meaningful comparison with the maximum allowed conversion, the equilibrium line in Fig. 12a corresponds to the maximum recorded temperature in the bed, i.e., 390 °C, which is a more representative state than the one considered for the inlet bed temperature. In any case, the measured temperature gradient is higher than the one attained under the same conditions in the previous experiments, which can be ascribed to the prolonged time-on-stream employed in the final experiment compared to the previous, short-term experiments (with a total duration of less than 12 h).

3.2.5. Spent catalyst characterization

Lastly, the morphology of the used catalyst (after both the on/off reaction cycles and the 75-h stability test) was examined in order to detect possible morphological changes. Intriguingly, SEM images demonstrated the excellent adhesion of the wash-coat, with the absence of cracks for all localized catalytic pellets, irrespective of their position in the catalyst bed (Fig. 13). Also, neither micro- or macro-cracks nor exfoliation were observed on the pellet wash-coat surface as well as in the Ni/CeO_2-NZP interface. At the same time, SEM-EDS spot analysis (see + in Fig. 13) confirmed the nominal Ni loading of 7.9 ± 0.7 wt.% in

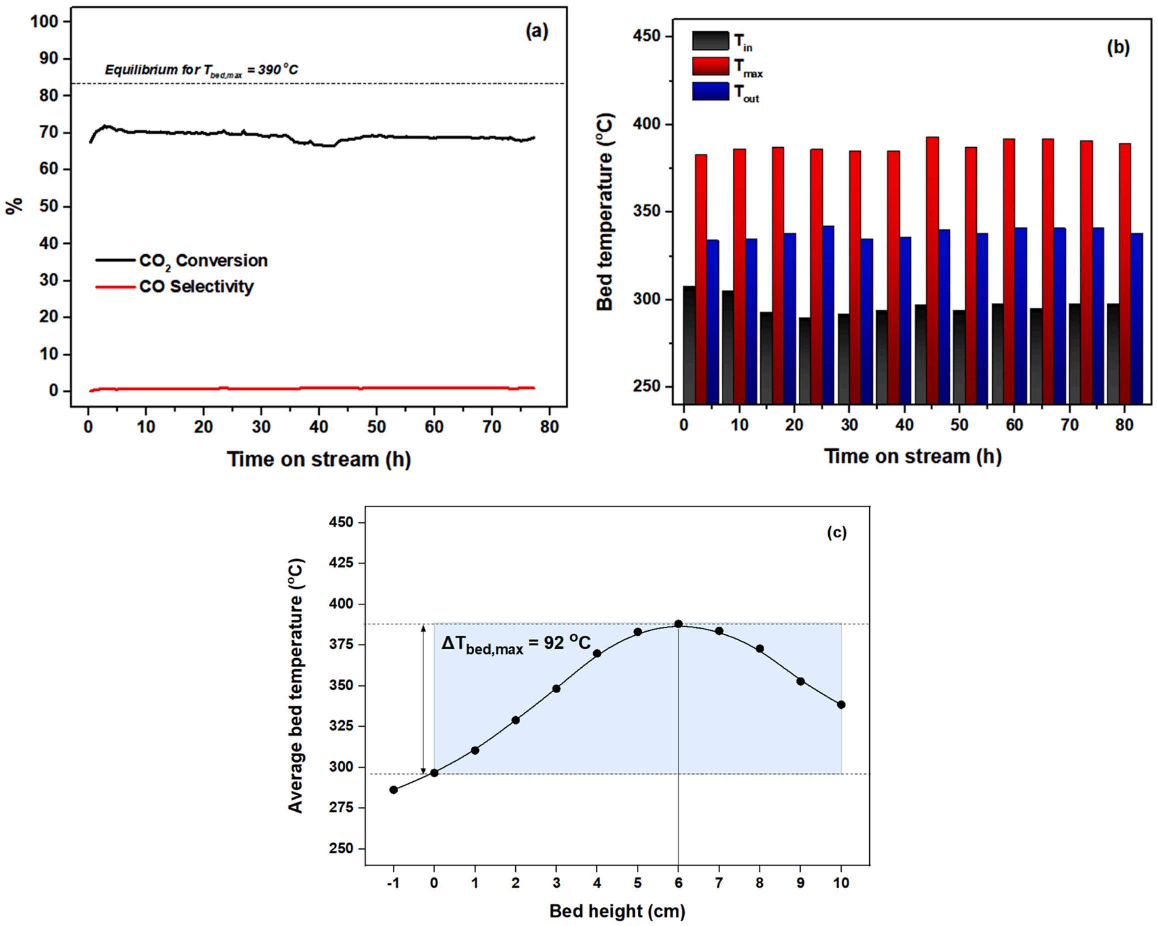

Fig. 12. Results from the stability test: (a) CO_2 conversion and CO selectivity, (b) Time-dependent values of the minimum, maximum and average bed temperature and (c) steady-state bed temperature profile.

the wash-coat and is in very good agreement with the corresponding result from the fresh catalyst (Fig. 3). The latter is also corroborated by ICP-AES measurements of the Ni content in both the fresh and spent structured catalysts taken from the inlet, middle and outlet parts of the catalytic bed. Indeed, a value of ca. 0.5 ± 0.05 wt.% Ni was measured in all cases, conducive of the stability of the sample and indicative of negligible nickel loss in the spent sample. The deviation from the nominal value may be directly attributable to the limitations of the ICP-AES method in such low Ni loading values, namely the solubility extent of nickel species during analysis and/or the interfering presence of the constituent metals in the NZP-type ceramic substrate.

Moreover, elemental mapping was carried out in the vicinity of the catalytic layer deposited on the perimeter of the ceramic sample in order to identify the localization of the main constituents of the structured catalyst (Fig. 14). Practically, Ce and Ni are foreseen as the main elements of the catalytic material deposited on the substrate, Ba and P are two of the main ingredients of the NZP-type ceramic substrate, whereas O is expected to be present all over the sample due to the oxide nature of all phases present in the structured catalyst. Indeed, the presence of Ce and Ni is evident in the coating area, while minor amounts are also present in the inner body of the pellet, whereas Ba and P are practically present only in the inner layer. This is attributed to the exceptionally highly porous and sponge-like morphology of this material (as seen also in Fig. 3a) and the interconnected porous channels that allow transportation to the inner part.

Therefore, considering the reported remarkable catalytic activity (Figs. 4 and 12) and the fact that significant temperature gradients were monitored in the various catalytic experiments (see Fig. 5), it is inferred that the combination of the ceramic NZP substrate and the active Ni/CeO_2-NR phase results in a bifunctional formulation that exhibits excellent properties as structured catalyst for enhanced and stable CO_2-to-CH_4 scaled-up activity.

3.2.6. Outlooks

The above findings clearly showcase that the remarkable lab-scale CO_2 methanation activity of the powder Ni/CeO_2-NR catalyst was largely maintained in a scaled-up process employing the wash-coating of the active phase into a porous NZP ceramic substrate as the structured catalyst. Also, the structured catalyst demonstrated remarkable stability even after several on/off reaction cycles and critically even after 75 h on stream under quasi-isothermal conditions, evidenced by the low deactivation rate and most importantly from the absence of morphological and structural alterations between the fresh and spent samples. Equally importantly, the as-prepared pellet catalyst exhibited an almost 5-fold increase in terms of methane productivity rate per unit mass of Ni compared to the powder sample, demonstrating the augmented utilization of the active phase in the structured pellet catalyst, paving the way for the development of a cost-effective structured catalyst formulation for CO_2 methanation process at practical scales. This may prove very beneficial in terms of the process feasibility prior to implementation and especially in scenarios were nickel or ceria (or even both) are considered as critical materials or in the case that catalyst production cost covers a considerable share of the total economics.

Ergo, regarding the implementation of the presented results, future studies involving evaluation of the catalyst at larger scales must initially take into consideration the significant effect of bed temperature gradients towards product distribution. Indeed, temperature control in a highly exothermic reaction progressing under increased conversion

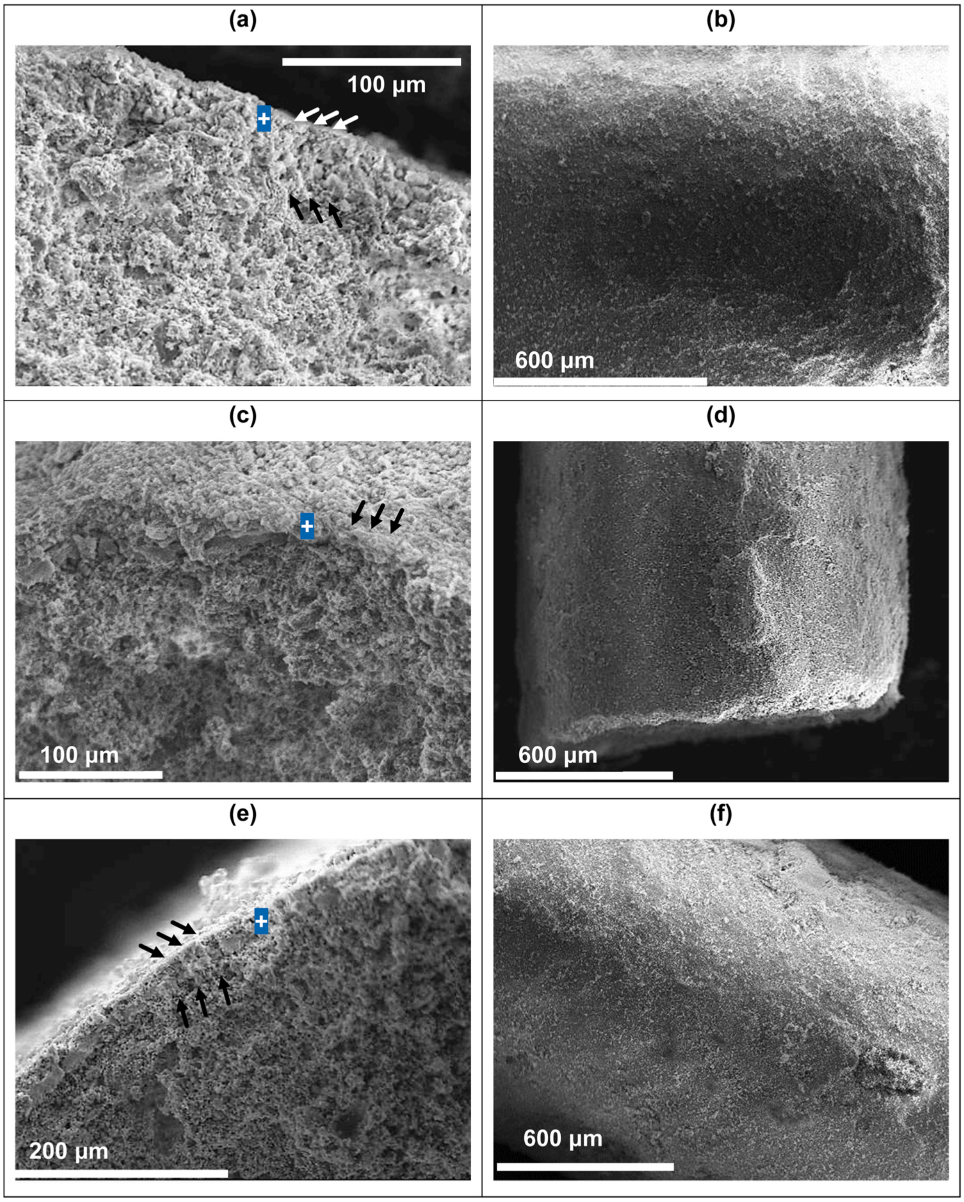

Fig. 13. SEM pictures of used catalyst pellets from the reactor up to 3 cm from inlet (a, b), 5–7 cm from inlet (c, d) and near the outlet of reactor bed over 8 cm (e, f). Wash-coat cross sectional view (a, c, e) and top view (b, d, f). Arrows point towards the wash-coat and + denotes the spot where EDS analysis was carried out.

values close to equilibrium, such as the Ni-catalyzed CO_2 methanation, is of utmost importance in a larger scale, where mass and heat transfer phenomena are expected to be even more prominent. To this end, the addition of a reactor cooling system (e.g., via water-cooling or a phase-change material) or a configuration involving two or more reactors in series with intermediate cooling and/or partial product recycle should be considered so as to ensure operation under quasi-isothermal conditions at each reactor. These measures will practically minimize catalyst sintering due to overheating, as well as improving the overall conversion by operating close to favorable thermodynamic conditions for CO_2 methanation and avoiding the formation of by-product CO.

Also, it is imperative that stability test under longer reaction times (several weeks in duration) are conducted in order to better assess the long-term thermal and structural stability of the catalyst. Moreover, within the scope of implementing the developed catalyst in a large-scale process, the effect of impurities in the reaction feed must also be assessed. Therefore, future experiments must be designed in order to account for the presence of various contaminants in the reactant feed with known deleterious effect on the catalyst, most prominently H_2S, NO_x and chlorine species. Lastly, considering the recycle of products in a real, multi-reactor process, the effect of CH_4 and H_2O or even CO in the reaction feed should be evaluated in one-pass catalytic tests.

4. Conclusions

In the present work we reported on the development of a structured catalyst employing Ni/CeO_2-nanorods as active phase, which was wash-coated on NZP-type ceramic pellets. The structured formulation was catalytically assessed in scale-up CO_2 methanation experiments (with a bed volume scaling factor of 65:1 compared to lab-scale studies), following the remarkable activity of the powder catalyst in our previous lab-scale study. It was disclosed that the as-prepared catalyst was associated with enhanced porous structure that facilitated the successful penetration of the active phase into the pores of the NZP substrate. As for the catalytic activity, increased one-pass CO_2 conversion values were demonstrated under variable reaction conditions, namely inlet temperature, gas hourly space velocity and H_2:CO_2 ratio. Additionally, it was shown that under a high-GHSV regime, the increased gaseous flow could

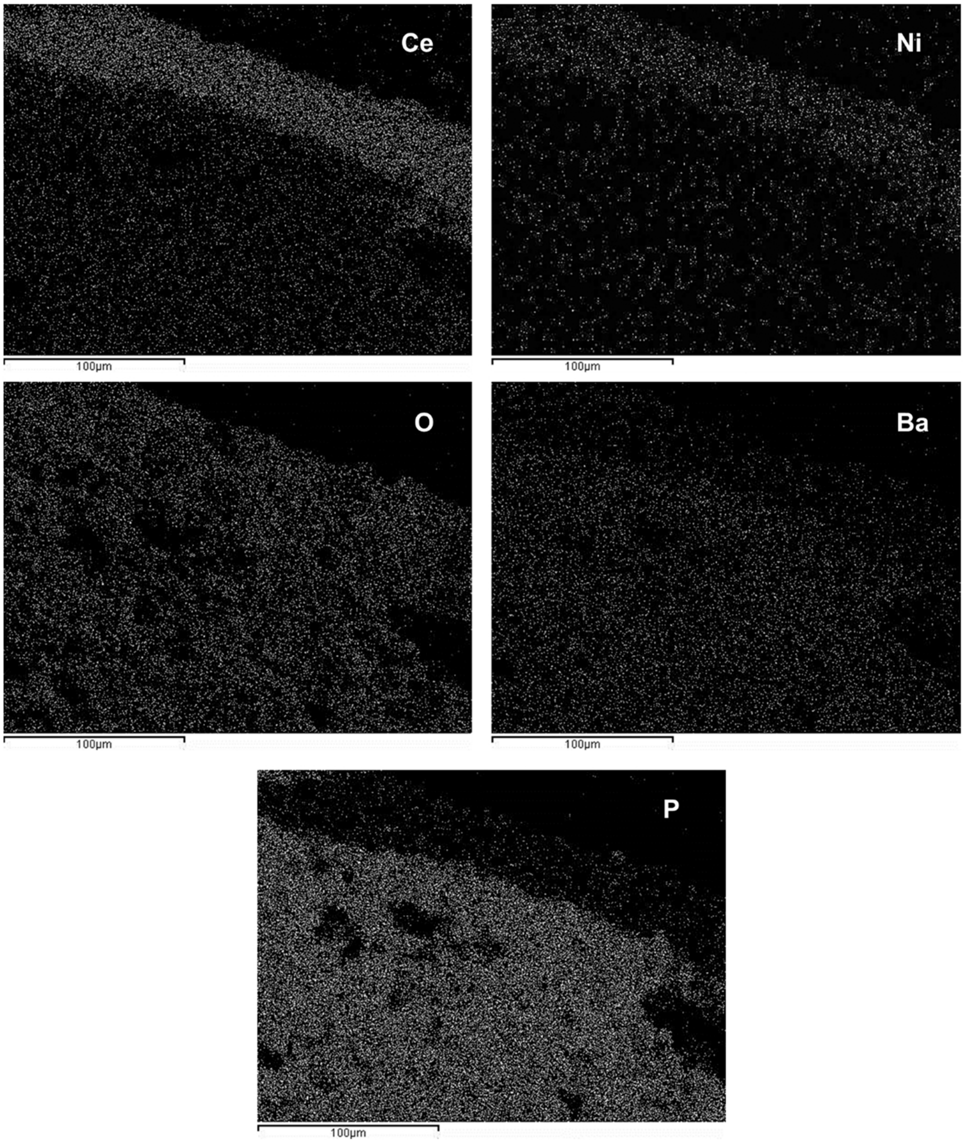

Fig. 14. Elemental mapping of the used catalyst pellets.

not effectively dissipate the generated heat by the exothermic methanation outwards from the bed, thereby leading to the development of higher bed temperature, resulting in increased CO selectivity. Collectively, it was demonstrated that the presence of both the active phase and the NZP-type substrate in a facilely synthesized and successfully wash-coated structured pellet catalyst acted synergistically towards attaining high CO_2-to-CH_4 yields under conditions that exceed the differential regime employed in micro-scale experiments.

CRediT authorship contribution statement

Georgios Varvoutis: Conceptualization, Investigation, Methodology, Software, Writing – original draft, Formal analysis. **Athanasios Lampropoulos:** Investigation, Visualization, Software. **Paraskevi Oikonomou:** Investigation, Methodology, Formal analysis. **Constantina-Dia Andreouli:** Resources, Supervision, Funding acquisition, Methodology. **Vassilis Stathopoulos:** Investigation, Methodology, Formal analysis. **Maria Lykaki:** Investigation, Methodology, Formal analysis. **George E. Marnellos:** Project administration, Supervision, Funding acquisition, Validation, Writing – review & editing. **Michalis Konsolakis:** Project administration, Supervision, Funding acquisition, Validation, Conceptualization, Writing – review & editing.

Declaration of Competing Interest

The authors declare that there is no known competing financial interest or personal relationship that could have influenced the work reported herein.

Data Availability

Data will be made available on request.

Acknowledgments

This research has been co-financed by the European Union NextGenerationEU under the call RESEARCH – CREATE – INNOVATE 16971 Recovery and Resilience Facility (Project code: TAEDK-06169).

Appendix A. Supporting information

Supplementary data associated with this article can be found in the online version at doi:10.1016/j.jcou.2023.102425.

References

[1] IPCC, Climate Change 2021 – The Physical Science Basis, 2021.

[2] J. Yan, Z. Zhang, Carbon capture, utilization and storage (CCUS), Appl. Energy 235 (2019) 1289–1299, https://doi.org/10.1016/j.apenergy.2018.11.019.

[3] A. Rafiee, K. Rajab Khalilpour, D. Milani, M. Panahi, Trends in CO_2 conversion and utilization: a review from process systems perspective, J. Environ. Chem. Eng. 6 (2018) 5771–5794, https://doi.org/10.1016/j.jece.2018.08.065.

[4] A. Antenucci, G. Sansavini, Extensive CO_2 recycling in power systems via power-to-gas and network storage, Renew. Sustain. Energy Rev. (2019), https://doi.org/10.1016/j.rser.2018.10.020.

[5] F. Gutiérrez-Martín, L.M. Rodríguez-Antón, Power-to-SNG technology for energy storage at large scales, Int. J. Hydrog. Energy 41 (2016) 19290–19303, https://doi.org/10.1016/j.ijhydene.2016.07.097.

[6] L.M. Romeo, M. Bailera, Design configurations to achieve an effective CO_2 use and mitigation through power to gas, J. CO_2 Util. 39 (2020), 101174, https://doi.org/10.1016/j.jcou.2020.101174.

[7] K. Kanellopoulos, S. Busch, D.F. M, Blending hydrogen from electrolysis into the European gas grid, 2022. ⟨https://doi.org/10.2760/908387⟩.

[8] I.A. Gondal, Hydrogen integration in power-to-gas networks, Int. J. Hydrog. Energy 44 (2019) 1803–1815, https://doi.org/10.1016/j.ijhydene.2018.11.164.

[9] J. Guilera, T. Boeltken, F. Timm, I. Mallol, A. Alarcón, T. Andreu, Pushing the limits of SNG process intensification: high GHSV operation at pilot scale, ACS Sustain. Chem. Eng. (2020), https://doi.org/10.1021/acssuschemeng.0c02642.

[10] V. Eveloy, T. Gebreegziabher, A review of projected power-to-gas deployment scenarios, Energies 11 (2018) 1824, https://doi.org/10.3390/en11071824.

[11] D. Hidalgo, J.M. Martín-Marroquín, Power-to-methane, coupling CO_2 capture with fuel production: an overview, Renew. Sustain. Energy Rev. 132 (2020), 110057, https://doi.org/10.1016/j.rser.2020.110057.

[12] E. Giglio, A. Lanzini, M. Santarelli, P. Leone, Synthetic natural gas via integrated high-temperature electrolysis and methanation: Part I-energy performance, J. Energy Storage 1 (2015) 22–37, https://doi.org/10.1016/j.est.2015.04.002.

[13] A. Mazza, E. Bompard, G. Chicco, Applications of power to gas technologies in emerging electrical systems, Renew. Sustain. Energy Rev. 92 (2018) 794–806, https://doi.org/10.1016/j.rser.2018.04.072.

[14] C. Wulf, A. Schreiber, P. Zapp, Review of power-to-gas projects in Europe, Energy Procedia 155 (2018) 191, https://doi.org/10.1016/j.egypro.2018.11.041.

[15] M. Bailera, P. Lisbona, L.M. Romeo, S. Espatolero, Power to gas projects review: lab, pilot and demo plants for storing renewable energy and CO_2, Renew. Sustain. Energy Rev. 69 (2017) 292–312, https://doi.org/10.1016/j.rser.2016.11.130.

[16] T.A. Atsbha, T. Yoon, P. Seongho, C. Lee, A review on the catalytic conversion of CO_2 using H_2 for synthesis of CO, methanol, and hydrocarbons, J. CO_2 Util. 44 (2021), 101413, https://doi.org/10.1016/j.jcou.2020.101413.

[17] T.T.N. Vu, A. Desgagnés, M.C. Iliuta, Efficient approaches to overcome challenges in material development for conventional and intensified CO_2 catalytic hydrogenation to CO, methanol, and DME, Appl. Catal. A Gen. 617 (2021), https://doi.org/10.1016/j.apcata.2021.118119.

[18] Samrand Saeidi, S. Najari, V. Hessel, K. Wilson, F.J. Keil, P. Concepción, S.L. Suib, A.E. Rodrigues, Recent advances in CO_2 hydrogenation to value-added products — current challenges and future directions, Prog. Energy Combust. Sci. 85 (2021), 100905, https://doi.org/10.1016/j.pecs.2021.100905.

[19] A.M. Bahmanpour, M. Signorile, O. Kröcher, Recent progress in syngas production via catalytic CO_2 hydrogenation reaction, Appl. Catal. B Environ. 295 (2021), 120319, https://doi.org/10.1016/j.apcatb.2021.120319.

[20] W.K. Fan, M. Tahir, Recent trends in developments of active metals and heterogenous materials for catalytic CO_2 hydrogenation to renewable methane: a review, J. Environ. Chem. Eng. 9 (2021), 105460, https://doi.org/10.1016/j.jece.2021.105460.

[21] R.P. Ye, J. Ding, W. Gong, M.D. Argyle, Q. Zhong, Y. Wang, C.K. Russell, Z. Xu, A. G. Russell, Q. Li, M. Fan, Y.G. Yao, CO_2 hydrogenation to high-value products via heterogeneous catalysis, Nat. Commun. 10 (2019), https://doi.org/10.1038/s41467-019-13638-9.

[22] C. Lv, L. Xu, M. Chen, Y. Cui, X. Wen, Y. Li, C.E. Wu, B. Yang, Z. Miao, X. Hu, Q. Shou, Recent progresses in constructing the highly efficient Ni based catalysts with advanced low-temperature activity toward CO_2 methanation, Front. Chem. 8 (2020) 1–32, https://doi.org/10.3389/fchem.2020.00269.

[23] L. Shen, J. Xu, M. Zhu, Y.-F. Han, Essential role of the support for nickel-based CO_2 methanation catalysts, ACS Catal. (2020) 14581–14591, https://doi.org/10.1021/acscatal.0c03471.

[24] G. Varvoutis, M. Lykaki, S. Stefa, E. Papista, S.A.C. Carabineiro, G.E. Marnellos, M. Konsolakis, S.A.C. Carabineiro, Remarkable efficiency of Ni supported on hydrothermally synthesized CeO_2 nanorods for low-temperature CO_2 hydrogenation to methane, Catal. Commun. 142 (2020), 106036, https://doi.org/10.1016/j.catcom.2020.106036.

[25] G. Varvoutis, M. Lykaki, S. Stefa, V. Binas, G.E. Marnellos, M. Konsolakis, Deciphering the role of Ni particle size and nickel-ceria interfacial perimeter in the low-temperature CO_2 methanation reaction over remarkably active Ni/CeO_2 nanorods, Appl. Catal. B Environ. 297 (2021), 120401, https://doi.org/10.1016/j.apcatb.2021.120401.

[26] S. Danaci, L. Protasova, J. Lefevere, L. Bedel, R. Guilet, P. Marty, Efficient CO_2 methanation over Ni/Al_2O_3 coated structured catalysts, Catal. Today 273 (2016) 234–243, https://doi.org/10.1016/j.cattod.2016.04.019.

[27] F. Kapteijn, J.A. Moulijn, Structured catalysts and reactors – perspectives for demanding applications, Catal. Today 383 (2022) 5–14, https://doi.org/10.1016/j.cattod.2020.09.026.

[28] A. Cybulski, J.A. Moulijn. Structured Catalysts and Reactors, Second edi., CRC Press, 2005 https://doi.org/10.1201/9781420028003.

[29] P.K. Pandis, D.E. Perros, V.N. Stathopoulos, Doped apatite-type lanthanum silicates in CO oxidation reaction, Catal. Commun. 114 (2018) 98–103, https://doi.org/10.1016/j.catcom.2018.06.017.

[30] P.K. Pandis, E. Xenogiannopoulou, P.M. Sakkas, G. Sourkouni, C. Argirusis, V. N. Stathopoulos, Compositional effect of Cr contamination susceptibility of $La_{9.83}Si_{6-x-y}Al_xFe_yO2_{6\pm\delta}$ apatite-type SOFC electrolytes in contact with CROFER 22 APU, RSC Adv. 6 (2016) 49429–49435, https://doi.org/10.1039/C6RA02025A.

[31] H.L. Huynh, W.M. Tucho, Z. Yu, Structured NiFe catalysts derived from in-situ grown layered double hydroxides on ceramic monolith for CO_2 methanation, Green Energy Environ. 5 (2020) 423–432, https://doi.org/10.1016/j.gee.2020.09.004.

[32] H.L. Huynh, W.M. Tucho, Q. Shen, Z. Yu, Bed packing configuration and hot-spot utilization for low-temperature CO_2 methanation on monolithic reactor, Chem. Eng. J. 428 (2021), 131106, https://doi.org/10.1016/j.cej.2021.131106.

[33] M. Frey, A. Bengaouer, G. Geffraye, D. Edouard, A.C. Roger, Aluminum open cell foams as efficient supports for carbon dioxide methanation catalysts: pilot-scale reaction results, Energy Technol. 5 (2017) 2078–2085, https://doi.org/10.1002/ente.201700188.

[34] F. Kosaka, T. Yamaguchi, Y. Ando, T. Mochizuki, H. Takagi, K. Matsuoka, Y. Fujishiro, K. Kuramoto, Effect of Ni content on CO_2 methanation performance with tubular-structured Ni-YSZ catalysts and optimization of catalytic activity for temperature management in the reactor, Int. J. Hydrog. Energy 45 (2020) 12911–12920, https://doi.org/10.1016/j.ijhydene.2020.02.221.

[35] Y. Dai, M. Xu, Q. Wang, R. Huang, Y. Jin, B. Bian, C. Tumurbaatar, B. Ishtsog, T. Bold, Y. Yang, Enhanced activity and stability of Ni/$La_2O_2CO_3$ catalyst for CO_2 methanation by metal-carbonate interaction, Appl. Catal. B Environ. 277 (2020), 119271, https://doi.org/10.1016/j.apcatb.2020.119271.

[36] J.J.H.B. Sattler, J. Ruiz-Martinez, E. Santillan-Jimenez, B.M. Weckhuysen, Catalytic dehydrogenation of light alkanes on metals and metal oxides, Chem. Rev. 114 (2014) 10613–10653, https://doi.org/10.1021/cr5002436.

[37] S.-R. J, A. Sepulveda-Escribano, F. Rodriguez-Reinoso, Bimetallic PtSn/C catalysts promoted by ceria: application in the nonoxidative dehydrogenation of isobutane, J. Catal. 246 (2007) 158–165, https://doi.org/10.1016/j.jcat.2006.12.004.

[38] P. Oikonomou, C. Dedeloudis, C.J. Stournaras, C. Ftikos, [NZP]: a new family of ceramics with low thermal expansion and tunable properties, J. Eur. Ceram. Soc. 27 (2007) 1253–1258, https://doi.org/10.1016/j.jeurceramsoc.2006.04.021.

[39] V.I. Pet'kov, E.A. Asabina, Thermophysical properties of NZP ceramics (a review), Glas. Ceram. 61 (2004) 233–239, https://doi.org/10.1023/B:GLAC.0000048353.42467.0a.

[40] D.K. Agrawal, C.-Y. Huang, H.A. McKinstry, NZP: a new family of low-thermal expansion materials, Int. J. Thermophys. 12 (1991) 697–710, https://doi.org/10.1007/BF00534225.

[41] C. Stournaras, P. Oikonomou, C. Andreouli, An environmentally friendly method for the production of NZP ceramic s with controlled characteristics, GR 20170100205, 2017.

[42] A. Vita, C. Italiano, L. Pino, M. Laganà, M. Ferraro, V. Antonucci, High-temperature CO_2 methanation over structured Ni/GDC catalysts: performance and scale-up for power-to-gas application, Fuel Process. Technol. 202 (2020), 106365, https://doi.org/10.1016/j.fuproc.2020.106365.

[43] A. Ricca, L. Truda, V. Palma, Study of the role of chemical support and structured carrier on the CO_2 methanation reaction, Chem. Eng. J. 377 (2019), 120461, https://doi.org/10.1016/j.cej.2018.11.159.

[44] H.L. Huynh, Z. Yu, CO_2 methanation on hydrotalcite-derived catalysts and structured reactors: a review, Energy Technol. 8 (2020), https://doi.org/10.1002/ente.201901475.

[45] M. Konsolakis, M. Lykaki, S. Stefa, S.A.C. Carabineiro, G. Varvoutis, E. Papista, G. E. Marnellos, CO_2 hydrogenation over nanoceria-supported transition metal catalysts: role of ceria morphology (nanorods versus nanocubes) and active phase nature (Co versus Cu), Nanomaterials 9 (2019) 1739, https://doi.org/10.3390/nano9121739.

[46] Y. Zhuang, D.S.A. Simakov, Autothermal CO_2 hydrogenation reactor for renewable natural gas generation: experimental proof-of-concept, React. Chem. Eng. (2022), https://doi.org/10.1039/d2re00236a.

[47] F. Kosaka, T. Yamaguchi, Y. Ando, T. Mochizuki, H. Takagi, K. Matsuoka, K. Kuramoto, Thermal management of CO_2 methanation with axial staging of active metal concentration in Ni-YSZ tubular catalysts, Int. J. Hydrog. Energy 46 (2021) 4116–4125, https://doi.org/10.1016/j.ijhydene.2020.10.247.

[48] G. Varvoutis, S.A. Karakoulia, M. Lykaki, S. Stefa, V. Binas, G.E. Marnellos, M. Konsolakis, Support-induced modifications on the CO_2 hydrogenation performance of Ni/CeO_2: the effect of ZnO doping on CeO_2 nanorods, J. CO_2 Util. 61 (2022), 102057, https://doi.org/10.1016/j.jcou.2022.102057.

[49] G. Varvoutis, M. Lykaki, E. Papista, S.A.C. Carabineiro, A.C. Psarras, G. E. Marnellos, M. Konsolakis, Effect of alkali (Cs) doping on the surface chemistry and CO_2 hydrogenation performance of CuO/CeO_2 catalysts, J. CO_2 Util. 44 (2021), 101408, https://doi.org/10.1016/j.jcou.2020.101408.

[50] S. Danaci, L. Protasova, V. Middelkoop, N. Ray, M. Jouve, A. Bengaouer, P. Marty, Scaling up of 3D printed and Ni/Al_2O_3 coated reactors for CO_2 methanation, React. Chem. Eng. 4 (2019) 1318–1330, https://doi.org/10.1039/C9RE00092E.

[51] Y. Dai, M. Xu, Q. Wang, R. Huang, Y. Jin, B. Bian, C. Tumurbaatar, B. Ishtsog, T. Bold, Y. Yang, Enhanced activity and stability of Ni/$La_2O_2CO_3$ catalyst for CO_2 methanation by metal-carbonate interaction, Appl. Catal. B Environ. 277 (2020), 119271, https://doi.org/10.1016/j.apcatb.2020.119271.

[52] L. Lin, S. Yao, N. Rui, L. Han, F. Zhang, C.A. Gerlak, Z. Liu, J. Cen, L. Song, S. D. Senanayake, H.L. Xin, J.G. Chen, J.A. Rodriguez, Conversion of CO_2 on a highly active and stable Cu/FeOX/CeO_2 catalyst: tuning catalytic performance by oxide-

oxide interactions, Catal. Sci. Technol. 9 (2019) 3735–3742, https://doi.org/10.1039/c9cy00722a.